Delamination of an elastic film from an elastic-plastic substrate during adhesive contact loading and unloading

Z. Song, K. Komvopoulos

PII: S0020-7683(13)00093-0
DOI: http://dx.doi.org/10.1016/j.ijsolstr.2013.03.002
Reference: SAS 7923

To appear in: *International Journal of Solids and Structures*

Received Date: 28 October 2012
Revised Date: 9 February 2013

Please cite this article as: Song, Z., Komvopoulos, K., Delamination of an elastic film from an elastic-plastic substrate during adhesive contact loading and unloading, *International Journal of Solids and Structures* (2013), doi: http://dx.doi.org/10.1016/j.ijsolstr.2013.03.002

Delamination of an elastic film from an elastic-plastic substrate during adhesive contact loading and unloading

Z. Song, K. Komvopoulos*

Department of Mechanical Engineering, University of California, Berkeley, California 94720, USA

Abstract

Adhesive contact between a rigid sphere and an elastic film on an elastic-perfectly plastic substrate was examined in the context of finite element simulation results. Surface adhesion was modeled by nonlinear springs obeying a force-displacement relationship governed by the Lennard-Jones potential. A bilinear cohesive zone law with prescribed cohesive strength and work of adhesion was used to simulate crack initiation and growth at the film/substrate interface. It is shown that the unloading response consists of five sequential stages: elastic recovery, interface damage (crack) initiation, damage evolution (delamination), film elastic bending, and abrupt surface separation (jump-out), with plastic deformation in the substrate occurring only during damage initiation. Substrate plasticity produces partial closure of the cohesive zone upon full unloading (jump-out), residual tensile stresses at the front of the crack tip, and irreversible downward bending of the elastic film. Finite element simulations illustrate the effects of minimum surface separation (i.e., maximum compressive surface force), work of adhesion and cohesive strength of the film/substrate interface, substrate yield strength, and initial crack size on the evolution of the surface force, residual deflection of the elastic film, film-substrate separation (debonding), crack-tip opening displacement, and contact instabilities (jump-in and jump-out) during a full load-unload cycle. The results of this study provide insight into the interdependence of contact instabilities and interfacial damage (cracking) encountered in layered media during adhesive contact loading and unloading.

Keywords: adhesion; cohesive zone; contact; crack; deformation; delamination; elasticity; finite element analysis; film; interfacial damage; plasticity; substrate

---

Corresponding author:
Tel: +1 510 642 2563, Fax: +1 510 643 5599, E-mail: kyriakos@me.berkeley.edu

Submitted to the *International Journal of Solids and Structures* on October 28, 2012; revised manuscript submitted on February 9, 2013.

1. Introduction

Thin films are widely used as protective coatings of various mechanical components possessing contact interfaces in order to maintain low friction and prevent wear of interacting surfaces. For example, thin diamond-like carbon films are used to protect the surfaces of hard disks and magnetic recording heads against mechanical wear caused by intermittent contact during the operation of hard-disk drives and to enhance the lifetime and reliability of contact-mode microelectromechanical systems (Komvopoulos, 1996, 2000, 2003; Smallwood et al., 2006). However, thin protective films may fail as a result of cracks caused by tensile contact stresses (Chai, 2003) or delamination at the film/substrate interface due to the mismatch of the film and substrate elastic-plastic properties (Bagchi and Evans, 1996). Marshall and Evans (1984) modeled a delaminating thin film as a rigidly clamped disk and evaluated the fracture toughness of the film/substrate interface using the indentation method. Drory and Hutchison (1996) analyzed conical indentation of a brittle film on a ductile substrate and proposed a method for determining the interface fracture toughness in terms of the applied normal load, delamination radius, film thickness, and mechanical properties of the film and the substrate materials.

Delamination mechanics is generally complicated by geometrical and material nonlinearities. In the presence of plasticity and the absence of an initial defect at the film/substrate interface, analytical solutions are cumbersome or even impossible. Thus, solutions can only be obtained by numerical methods, such as the finite element method (FEM). Xia et al. (2007) simulated normal contact between a rigid sphere and an elastic film on an elastic-plastic substrate using a cohesive zone model for the film/substrate interface and observed shear cracking outside the contact area beyond a critical indentation depth and tensile cracking at the interface below the center of contact upon unloading. Chen et al. (2009) used a FEM model to examine wedge indentation of a soft film on a hard substrate and determined the critical indentation load for crack initiation as a function of the interface toughness and strength, reporting a good agreement between experimental and FEM results of interface properties for wedge angles of 90° and 120°.

Although the previous studies have provided insight into contact-induced delamination in film/substrate systems, the effect of surface adhesion on the contact deformation was not considered. Pioneering adhesion studies of Johnson et al. (1971) and Derjaguin et al. (1975) have produced analytical models of elastic spherical contact, known as the JKR and the DMT model, respectively, which yield estimates of the pull-off force P_{off}, i.e., the force at the instant of full separation of the adhering elastic spheres during unloading. Tabor (1977) has argued that the JKR and DMT models represent extreme conditions of adhesion systems with $\mu \gg 5$ and $\mu \ll 0.1$, respectively, where $\mu = \left(\frac{RW^2}{E^{*2}\varepsilon^3}\right)^{1/3}$ is known as the Tabor parameter, where $R = \frac{R_1 R_2}{R_1 + R_2}$ is the reduced radius of curvature of two adhering spheres (1) and (2) with radius of curvature R_1 and R_2, respectively, W is the work of adhesion, $E^* = \left[\frac{1-\nu_1^2}{E_1} + \frac{1-\nu_2^2}{E_2}\right]^{-1}$ is the effective elastic modulus (E_1, E_2 and ν_1, ν_2 represent the elastic modulus and Poisson's ratio of spheres (1) and (2), respectively), and ε is the equilibrium interatomic distance. Maguis (1992) used the Dugdale approximation to describe the adhesive contact stress and obtained a solution of P_{off} in the range $0.1 \ll \mu \ll 5$, i.e., the transition range of the Tabor parameter between the DMT ($\mu \ll 0.1$) and the JKR ($\mu \gg 5$) solutions. Muller et al. (1980), Greenwood (1997), and Feng (2001) modeled the adhesive stress between contacting elastic spheres by a traction-separation law derived from the Lennard-Jones (LJ) potential and obtained numerical results that provide a smooth transition of the pull-off force between the JKR and the DMT solutions. Although the former solutions based on the LJ potential differ slightly from that reported by Maguis (1992), they reproduce adhesion-induced instability phenomena, i.e., instantaneous surface contact (jump-in) and separation (jump-out), which are often observed during the operation of microprobe instruments and suspended microstructures.

Nonlinear spring elements obeying a force-displacement constitutive relation derived from the LJ potential have been used in FEM studies to model adhesive contact either of a rigid plate with an elastic-plastic hemisphere (Du et al., 2007; Kadin et al., 2008) or a rigid sphere with an elastic-plastic half-space

(Song and Komvopoulos, 2011). These studies have shed light into the effects of various geometrical, loading, and material parameters on the evolution of P_{off} and the occurrence of contact instabilities. Eid et al. (2011) extended the FEM model of Du et al. (2007) to study adhesive contact between a rigid plate and an elastic-plastic layered hemisphere and observed a dependence of the adhesion force and contact radius on the maximum contact displacement (compressive force) and film thickness. Song and Komvopoulos (2013) analyzed single and repetitive normal contact between a rigid sphere and a hard elastic film bonded to an elastic-perfectly plastic substrate and obtained a multi-parameter map of brittle- and ductile-like surface separation of adhesive contacts.

Despite important information about the role of adhesion in contact deformation provided by the aforementioned studies, a comprehensive analysis of adhesion-induced delamination at film/substrate interfaces is still lacking. The objective of this study was to investigate the effect of surface adhesion (governed by the LJ potential) on interfacial delamination in elastic-plastic layered media, using a cohesive zone that obeys a bilinear traction-separation constitutive law to model the film/substrate interface. FEM results provide insight into interface damage (crack) initiation and evolution (delamination) during a full load-unload cycle. Irreversible film bending and crack-tip opening and closure occurring before and after full unloading (jump-out) are interpreted in the context of the residual cohesive zone and the energy release rate. Numerical solutions elucidate the effects of minimum surface separation (maximum compressive force), substrate yield strength, interface work of adhesion, cohesive strength, and preexisting crack size on interface damage initiation and delamination.

2. Contact model

Fig. 1 shows the axisymmetric problem under consideration, i.e., a rigid sphere of radius R in close proximity with a half-space consisting of an elastic film of thickness t and a semi-infinite elastic-perfectly plastic substrate. The FEM mesh of the substrate and the film comprises 4,096 and 26,656 axisymmetric, four-node, linear, isoparametric elements with a total of 4,618 and 27,170 nodes, respectively. All nodes at the bottom boundary and the axis of symmetry ($r = 0$) are constrained against

displacement in the z - and r -direction, respectively. To accurately capture the evolution of contact at the film surface and the delamination of the film from the substrate, a refined mesh is used at the film surface and the film/substrate interface, with a node-to-node distance d approximately equal to $0.003R$ and $0.006R$, respectively. Adhesion between the sphere and the film is modeled by nonlinear spring elements obeying a traction-separation relation governed by the LJ potential. Details about the nonlinear spring constitutive equation can be found elsewhere (Song and Komvopoulos, 2011). All of the contact simulations were performed with the FEM code ABAQUS (version 6.9EF).

Coherence at the film/substrate interface is represented by a cohesive-zone law (Tvergaard and Hutchinson, 1994, 1996), which allows the film to separate from the substrate in order to simulate crack initiation and growth. Fig. 2 shows a schematic of the bilinear traction-separation law of the cohesive interface. The figure shows the effective surface traction $\sigma_{ef} = \sqrt{\sigma_n^2 + \sigma_t^2 + \sigma_s^2}$ as a function of the effective interfacial separation $h_{ef} = \sqrt{h_n^2 + h_t^2 + h_s^2}$, where subscript n denotes the normal direction at the film/substrate interface and t and s denote the two in-plane orthogonal directions, σ_c is the cohesive strength, h^* is the effective interfacial separation for damage (crack) initiation, and h_c is the effective interfacial separation for failure, i.e., permanent film separation from the substrate (delamination).

Before the initiation of interfacial damage ($\sigma_{ef} < \sigma_c$), the traction-separation law is given by

$$\begin{bmatrix} \sigma_n \\ \sigma_t \\ \sigma_s \end{bmatrix} = \begin{bmatrix} k_n & 0 & 0 \\ 0 & k_t & 0 \\ 0 & 0 & k_s \end{bmatrix} \begin{bmatrix} h_n \\ h_t \\ h_s \end{bmatrix} \quad (1)$$

where k_n, k_t, and k_s represent the interface stiffness in the normal and the two in-plane directions, respectively. In the present analysis, the interface is assumed to be isotropic ($k_n = k_t = k_s = k$), and Eq. (1) reduces to the linear relation $\sigma_{ef} = kh_{ef}$ (Fig. 2).

Interfacial damage commences when the effective traction reaches the cohesive strength, i.e.,

$$\sigma_{ef} = \sqrt{\sigma_n^2 + \sigma_t^2 + \sigma_s^2} = \sigma_c \tag{2}$$

Thus, the critical effective interfacial separation for the initiation of interfacial damage is given by

$$h^* = \sigma_c / f_{ic} \tag{3}$$

The effective surface traction σ_{ef} decrease linearly as h_{ef} increases in the range $h_{ef} \geq h^*$ and eventually vanishes when $h_{ef} = h_c$. At that juncture, permanent separation of the film from the substrate (delamination) commences and the interfacial failure criterion is given by

$$\Gamma_n + \Gamma_t + \Gamma_s = \Gamma_c \tag{4}$$

where Γ_n, Γ_t, and Γ_s represent the work of surface traction on conjugate relative displacement in the normal and two in-plane (shear) directions and Γ_c is the interfacial work of adhesion (toughness), given by

$$\Gamma_c = \frac{1}{2}\sigma_c h_c \tag{5}$$

Eq. (5) indicates that Γ_c is an intrinsic interface property that is independent of the mode of surface separation (fracture).

The effective surface traction-separation law at the film/substrate interface of the layered medium can be expressed as

$$\sigma_{ef} = \begin{cases} \left(\frac{h_{ef}}{h^*}\right)\sigma_c & (0 \leq h_{ef} \leq h^*) \\ \left(\frac{h_c - h_{ef}}{h_c - h^*}\right)\sigma_c & (h^* \leq h_{ef} \leq h_c) \\ 0 & (h_{ef} \geq h_c) \end{cases} \tag{6}$$

Eq. (6) shows a linear increase of σ_{ef} with h_{ef} for $h_{ef} \leq h^*$, implying purely elastic deformation at the interface, whereas for $h^* \leq h_{ef} \leq h_c$, σ_{ef} decreases linearly from σ_c to zero with the increase of h_{ef} due to the accumulation of damage at the film/substrate interface. Interfacial damage

produces a unloading path (CO) that does not coincide with the loading path (OA). Film-substrate delamination (full damage) produces a locally traction-free interface. In all simulations, h^* (on the order of the interatomic distance) is fixed, while h_c (3–10 times h^*) is varied with σ_c and Γ_c according to Eq. (5).

Special simulations were performed to confirm the validity of the FEM mesh used in the present analysis. First, adhesive contact between a rigid sphere and a layered elastic medium with film and substrate elastic modulus E_f and E_s, respectively was simulated with the present mesh for varied in the range of $E_f = E_s =$ 5–1000 GPa, $\bar{\sigma}_c = \frac{\sigma_c \delta^*}{W} = 1.5 \times 10^3$, and $\bar{\Gamma}_c = \frac{\Gamma_c}{W} = 2.5 \times 10^3$. A relatively high cohesive strength was used in these simulations to minimize the effect of interfacial separation on the deformation of the layered medium and, thus, facilitate the evaluation of the surface mesh. Fig. 3(a) shows a comparison of the dimensionless pull-off force $\bar{P}_{off} = \frac{P_{off}}{2\pi RW}$ versus the Tabor parameter μ obtained with the present FEM model and solutions from previous empirical (Carpick et al., 1999) and numerical (Wu, 2008) analyses of adhesive elastic contact. It is noted that $\bar{P}_{off}$ asymptotically increases from 0.75 (JKR solution) to 1.0 (DMT solution) with the decrease of μ. In addition, the FEM results closely follow the solutions of Wu and Carpick et al. Second, adhesive contact between a rigid sphere and a layered elastic medium was simulated with FEM meshes having an interface mesh size d = $0.003R$, $0.006R$, $0.012R$, and $0.024R$ for $E_f = E_s =$ 50 GPa, $\bar{\sigma}_c = 0.15$, and $\bar{\Gamma}_c = 0.25$. Fig. 3(b) shows the dimensionless surface force $\bar{F} = \frac{P}{2\pi RW}$ versus the dimensionless surface separation $\bar{\delta} = \frac{\delta}{\delta^*}$. The very close agreement of the FEM results obtained with different mesh sizes confirms the independence of the simulation results on the interface mesh size (d = $0.006R$) of the present model. The good agreement between FEM results and solutions of earlier studies (Fig. 3(a)) and the independence of the FEM results on the size of the interface mesh (Fig. 3(b)) illustrate the suitability of the FEM mesh used in the present analysis.

3. Results and discussion

Interface delamination was analyzed by the mixed-mode cohesive zone model described in the previous section. However, because the dominant mode in adhesion-induced delamination during unloading is the tensile (opening) mode, the interfacial shearing displacement and the tangential traction are secondary compared to the crack-tip opening displacement and the normal traction, respectively, i.e., $\sigma_{ef} \approx \sigma_n = \sigma$ and $h_{ef} \approx h_n = h$. Thus, the results presented in this section are discussed in terms of the dominant normal traction σ and the interfacial separation within the cohesive zone h (or film-substrate normal separation).

Figs. 4(a) and 4(b) show schematics of the deformed layered medium before and after full surface separation (jump-out), respectively. In general, three distinct interface regions can be observed before jump-out (Fig. 4(a)): a fully damaged (white) region of zero strength ($h \geq h_s$), representing an interfacial crack of radius a_c and crack-tip surface separation h_c, a partially damaged cohesive zone (gray) of strength less than σ_c ($h^* \leq h \leq h_s$), and an elastically stretched (red) region ahead of the damaged cohesive zone ($0 \leq h \leq h^*$). The fully damaged region (crack) together with the partially damaged cohesive zone represent a fictitious crack of radius a_{fc} and tip surface separation $h_{fc} = h^*$. After jump-out (Fig. 4(b)), full unloading yields a crack-tip opening displacement ($CTOD$), a residual fictitious crack of radius a_{fc}^{res}, and a maximum tensile stress at the crack tip σ_{max}. Although jump-out (full unloading) does not affect the crack radius, it reduces the radius of the elastically stretched (red) region and the damaged cohesive zone (gray) due to the elastic recovery of the film and the nonuniform plastic deformation at the substrate face of the cohesive zone, respectively. This produces a closed (blue) region of cohesive zone between the residual fictitious crack and the elastically stretched region. As a consequence, $a_{fc}^{res} \leq a_{fc}$ and $h_{fc}^{res} \leq h^*$. (Superscript "res" indicates "residual" parameters obtained after full unloading (jump-out).)

Results from displacement-control FEM simulations are presented and discussed next in terms of dimensionless parameters defined in Sect. 2, i.e., surface force $\overline{P}$, surface separation $\overline{\delta}$, cohesive strength $\overline{\sigma}_c$, interfacial work of adhesion (toughness) $\overline{\Gamma}_c$, and, in addition, minimum surface separation (corresponding to the maximum compressive force) $\overline{\delta}_{\min} = \frac{\delta_{\min}}{t}$, interfacial separation $\overline{\Delta} = \frac{\Delta}{h_c}$, film-substrate separation below the center of contact $\overline{\Delta}_o = \frac{\Delta_o}{h_c}$, residual film deflection at the center of contact $\overline{\delta}^{res} = \frac{\delta^{res}}{h_c}$, substrate yield strength $\overline{Y} = \frac{Y}{\sigma_c}$, film deflection at the crack-tip location $\overline{\Delta}_f = \frac{\Delta_f}{h_c}$, crack radius $\overline{a}_c = \frac{a_c}{t}$, fictitious crack radius $\overline{a}_{fc} = \frac{a_{fc}}{t}$, radius of the residual fictitious crack $\overline{a}_{fc}^{res} = \frac{a_{fc}^{res}}{t}$, closure of the residual fictitious crack $c = 1 - \left(\frac{a_{fc}^{res}}{a_{fc}}\right)^2$, and initial crack radius $\overline{a}_i = \frac{a_i}{t}$. The film-to-substrate elastic modulus ratio $\frac{E_f}{E_s}$ and the sphere radius-to-film thickness ratio $\frac{R}{t}$ are also important parameters. However, because the focus in the present study is on adhesive contact of layered media with films much stiffer than the substrate, typical of hard protective films used in hard-disk drives and microelectomechanical systems, all simulation results presented below are for $\frac{E_f}{E_s}$ = 10 and $\frac{R}{t}$ = 10. Hereafter, a positive (negative) surface force will be designated as a compressive (tensile) force.

3.1. Effect of minimum surface separation

Figs. 5(a) and 5(b) show the surface force $\overline{P}$ and corresponding film-substrate separation below the center of contact $\overline{\Delta}_o$, respectively, as functions of the surface separation $\overline{\delta}$ for $\overline{\Gamma}_c$ = 0.125, $\overline{Y}$ = 0.4, $\overline{\sigma}_c$ = 0.075, and $\overline{\delta}_{\min}$ = –0.5, –1.0, and –1.5. Since the three simulation cases demonstrate similar characteristics, the case of $\overline{\delta}_{\min}$ = –1.5 is used to describe the general loading (solid lines) and unloading (dashed lines) contact behavior. (For clarity, arrows indicating the loading direction (right to left) and the unloading direction (left to right) are only shown in this figure for $\overline{\delta}_{\min}$ = –1.5). For all

three simulation cases, the variation of $\bar{\Delta}_o$ with $\bar{\delta}$ during loading is shown by the barely visible response at the bottom of Fig. 5(b). Long-range surface attraction results in abrupt contact (jump-in) at a critical surface separation ($\bar{\delta} \approx$ 0.25), accompanied by the upward displacement of the layered medium, as evidenced by the sharp rise of a negative (tensile) surface force. The decrease of the surface separation beyond this point leads to the transition from tensile to compressive surface force and the downward displacement of the layered medium. The linear force response from the instant of contact to the minimum surface separation (point A) can be explained by a simple plate bending model. Because of the low yield strength of the substrate ($\bar{Y} = 0.125$) and the significantly higher elastic modulus of the film ($\frac{E_f}{E_s} = 10$), plastic deformation in the substrate below the center of contact yields a situation approximately analogous to the elastic bending of a circumferentially clamped circular plate (film) due to a normal force at its center point. Thus, the linear loading path seen in Fig. 5(a) is dominated by the bending behavior of the elastic film, not contact deformation. This attribution is supported by results for a layered medium with a high-yield strength substrate (section 3.2) demonstrating a nonlinear increase of $\bar{P}$ with $\bar{\delta}$, which is typical of contact deformation.

The development of a force hysteresis after full unloading indicates the occurrence of irreversible deformation, i.e., plastic deformation in the substrate and/or film debonding (delamination). Initial unloading is characterized by a purely linear elastic response (AB), with the film remaining fully bonded to the substrate ($\bar{\Delta}_o = 0$). Further retraction of the rigid sphere produces a nonlinear elastic-plastic force response (BC). This is attributed to plastic deformation in the substrate induced during loading that prevents further elastic recovery. As a consequence, large strain gradients develop at the film/substrate interface, resulting in a cohesive tensile stress ($\bar{\Delta}_o > 0$) that causes re-yielding in the substrate adjacent to the interface. Interface damage initiation commences at a critical surface separation ($\bar{\delta} \approx$ –0.8), as evidenced by the sharp change in slope of the force response (point C). Additional damage due to further unloading decreases the cohesive stress, resulting in the partial recovery of the upward displacement of

the substrate, which leads to delamination ($\bar{\Delta}_o$ = 1.0) and the decrease of the tensile surface force (CD). The subsequent increase of the tensile surface force (DE) is due to upward film bending. Abrupt surface separation (jump-out) (point E) leading to full unloading (point F) commences when further film deflection cannot be compensated by interfacial adhesion. Equivalent plastic strain contours in the highly deformed regions of the substrate adjacent to the interface (not shown here), corresponding to characteristic points of the unloading response for $\bar{\delta}_{min}$ = –1.5 shown in Fig. 5, confirmed that accumulation of plasticity in the substrate during unloading occurred only along the unloading path BC, indicating that the cause of substrate re-yielding was the increase of the cohesive stress with the film-substrate separation (path OA in Fig. 2).

Fig. 6(a) shows contours of the dimensionless residual normal stress $\bar{\sigma}_{zz}^{res} = \frac{\sigma_{zz}^{res}}{Y}$ for $\bar{\Gamma}_o$ = 0.125, $\bar{Y}$ = 0.4, $\bar{\sigma}_o$ = 0.075, and $\bar{\delta}_{min}$ = –1.5. Tensile stresses arise around the fictitious crack tip, whereas the stress field ahead of the fictitious crack tip is compressive. The presence of these regions of tensile and compressive residual stress can be explained by considering the evolution of plasticity in the substrate. Before jump-out (point E in Fig. 5), a cohesive zone exists at the crack-tip front because the plastically deformed substrate cannot follow the upward deflection of the elastic film (Fig. 4(a)). At the instant of jump-out (point F in Fig. 5), the surface force decreases abruptly to zero, resulting in the elastic spring-back of the film. However, plastic deformation in the substrate adjacent to the interface only allows partial crack closure (blue region in Fig. 4(b)). This produces a residual cohesive zone of smaller radius and lower tensile stress, which accounts for the residual tensile stress at the fictitious crack tip seen in Fig. 6(a). This residual tensile stress is responsible for the downward bending of the elastic film, quantified by the residual deflection δ^{res} at the center of contact (Fig. 4(b)). Fig. 6(b) shows a linear variation of the dimensionless residual film deflection $\bar{\delta}^{res}$ with $\bar{\delta}_{min}$ for $\bar{\Gamma}_o$ = 0.125, $\bar{Y}$ = 0.4, and $\bar{\sigma}_o$ = 0.075.

The crack-tip opening displacement $CTOD$ is a measure of the fracture toughness in classical fracture mechanics, because it is proportional to the energy release rate G and inversely proportional to the cohesive strength σ_c (Anderson, 1995). Fig. 7 shows the dimensionless crack-tip opening displacement $\beta = \frac{CTOD}{h_c}$ after jump-out as a function of $\bar{\vartheta}_{min}$ for $\bar{\Gamma}_c$ = 0.125, $\bar{Y}$ = 0.4, and $\bar{\sigma}_c$ = 0.075. The increase of β with $\bar{\vartheta}_{min}$ implies an increase of the fracture toughness with the minimum surface separation, which can be associated with the increase of crack-tip blunting with substrate plasticity. To interpret the dependence of β on $\bar{\vartheta}_{min}$, it is instructive to consider the energy release rate before and after jump-out. Just before jump-out (point E in Fig. 5), β = 1.0 and the energy release rate G_E consists of the elastic strain energy in the film U_f, the plastic strain energy in the substrate U_s, and the interface work of adhesion Γ_c, i.e., $G_E = U_f + U_s + \Gamma_c$. After jump-out (point F in Fig. 5), U_f is almost fully recovered (the film remains slightly deflected because of the tensile stress in the residual cohesive zone) and Γ_c is almost unchanged because the fictitious crack exhibits only partial closure, i.e., $G_F \approx U_s + \Gamma_c$. Thus, considering that $CTOD \propto G$, the dimensionless crack-tip opening displacement after surface separation (full unloading) can be expressed as

$$\beta \approx \left[1 + \frac{\frac{U_f}{U_s}}{1 + \frac{\Gamma_c}{U_s}}\right]^{-1} \tag{7}$$

As shown in Fig. 7, the film upward deflection at the crack-tip location $\bar{\Delta}_f$ (Fig. 4(a)) decreases with the increase of $\bar{\vartheta}_{min}$. This can be attributed to the accumulation of more plasticity in the substrate during loading with the increase of $\bar{\vartheta}_{min}$, resulting in more residual deformation upon unloading and, in turn, less upward deflection of the film. Thus, considering that U_f decreases with $\bar{\Delta}_f$ and that U_s increases with $\bar{\vartheta}_{min}$, the tendency for β to increase with $\bar{\vartheta}_{min}$ can be explained by Eq. (7).

3.2. Effect of substrate yield strength

Figs. 8(a) and 8(b) show the effect of the substrate yield strength $\bar{Y}$ on the variation of the surface force $\bar{P}$ and corresponding film-substrate separation below the center of contact $\bar{\Delta}_o$ with the surface separation $\bar{\delta}$, respectively, for $\bar{\Gamma}_e$ = 0.125, $\bar{\sigma}_e$ = 0.075, and $\bar{\vartheta}_{\min}$ = –1.0. As expected, the contact stiffness increases with the substrate yield strength. For $\bar{Y}$ = 10, the loading curve almost overlaps with the unloading curve, indicating negligible substrate plasticity or film delamination. The higher $\bar{\Delta}_o$ and $\bar{\delta}$ values at the instant of jump-out obtained for $\bar{Y}$ = 1.0 than 0.1 and 10 (Fig. 8(b)) suggest the existence of an intermediate yield strength range conducive to film delamination. This effect of the substrate yield strength can be better understood by considering the variation of the interfacial separation $\bar{\Delta}$ before (solid lines) and after (dashed lines) jump-out for $\bar{\Gamma}_e$ = 0.125, $\bar{Y}$ = 0.1, 1.0, and 10, $\bar{\sigma}_e$ = 0.075, and $\bar{\vartheta}_{\min}$ = –1.0, shown in Fig. 9. For $\bar{Y}$ = 0.1, the relatively high cohesive strength leads to significant plastic deformation in the substrate during unloading, which enhances the conformity of the deflected elastic film with the substrate (i.e., small $\bar{\Delta}$). For $\bar{Y}$ = 1.0, strain incompatibility at the interface due to the mismatch of the film and the substrate material properties leads to film delamination. For $\bar{Y}$ = 10, plastic deformation is negligible due to the high strength of the substrate and delamination commences before jump-out because the elastic deflection of the film caused by surface adhesion is compensated by the cohesive stress. However, film debonding from the substrate is less than that for $\bar{Y}$ = 1.0 because the residual deformation in the substrate is negligible. Consequently, the elastic deflection of the film is fully recovered upon jump-out, resulting in full crack closure. The condition of maximum interface delamination cannot be determined from only three simulation cases and also because other important parameters, particularly E_s and $\bar{\vartheta}_{\min}$, play an important role in film delamination. Nevertheless, considering the results shown in Fig. 9 and the opposite effects of excessive plasticity during unloading (low $\bar{Y}$) and negligible plasticity during loading (high $\bar{Y}$), maximum interface delamination should occur for an intermediate $\bar{Y}$ range.

3.3. Effect of interface work of adhesion

Figs. 10(a) and 10(b) show the surface force $\overline{P}$ and corresponding film-substrate separation below the center of contact $\overline{\Delta}_o$ as functions of the surface separation $\overline{\delta}$, respectively, for $\overline{\Gamma}_c$ = 0.125, 0.25, and 0.5, $\overline{Y}$ = 0.4, $\overline{\sigma}_c$ = 0.075, and $\overline{\delta}_{\min}$ = –1.0. In all three simulation cases, the variation of $\overline{\Delta}_o$ with $\overline{\delta}$ during loading (solid lines) is shown by the barely visible response at the bottom of Fig. 10(b). Characteristic points (similar to those shown in Fig. 5) are shown for $\overline{\Gamma}_c$ = 0.125. The loading response does not show a dependence on the work of adhesion of the film/substrate interface because the dominance of compressive deformation during loading prevents delamination even for a low work of adhesion ($\overline{\Gamma}_c$ = 0.125). This is also evidenced by the very small $\overline{\Delta}_o$ values obtained during loading (Fig. 10(b)). Similar to loading, unloading (dashed lines) does not show a dependence on the work of adhesion of the film/substrate interface initially (AB). In this stage of unloading, a cohesive zone does not form ($\overline{\Delta}_o = 0$) because the interface is still under compression. Further unloading induces localized film debonding characterized by a nonlinear force response (BC). Unloading up to the point of damage initiation ($\Delta_o \approx h^*$) is independent of $\overline{\Gamma}_c$ because h^* and $\overline{\sigma}_c$ are fixed in these simulation cases. However, upon the formation of a cohesive zone (point C), the unloading behavior shows a strong dependence on the interface work of adhesion. For $\overline{\Gamma}_c$ = 0.125, the surface force first decreases slightly (CD) and then gradually increases with further unloading up to the instant of jump-out (point E) when it decreases abruptly to zero (point F). Point D is not distinguishable in the simulation cases of $\overline{\Gamma}_c$ = 0.25 and 0.5 because the decrease in cohesive stress caused by the interfacial damage is limited by the relatively high $\overline{\Gamma}_c$ and h_c values (Eq. (5)). The slightly lower $\overline{P}$ and significantly higher $\overline{\Delta}_o$ values obtained at the instant of jump-out with higher $\overline{\Gamma}_c$ imply smaller surface separation at jump-out for higher interface strength.

Figs. 11(a) and 11(b) show the radius of the fictitious crack $\overline{a}_{fs}$ and the residual fictitious crack $\overline{a}_{fs}^{res}$ (points E and F, respectively, in Figs. 5 and 10) and the closure of the fictitious crack upon jump-out c as functions of the interface work of adhesion $\overline{\Gamma}_c$ for $\overline{Y}$ = 0.4, $\overline{\sigma}_c$ = 0.075, $\overline{\delta}_{\min}$ = –1.0, and similar

$\bar{F}_{off}$, as evidenced from Fig. 10. The monotonic decrease of $\bar{a}_{fc}$ and $\bar{a}_{fc}^{neg}$ with increasing $\bar{\Gamma}_c$ reveals an increase of the interface resistance against damage initiation ($h \gg h^*$) and delamination ($h \gg h_c$) for fixed $\bar{F}_{off}$. Fig. 11(b) shows that crack closure increases with interface work of adhesion, approaching asymptotically full closure (c = 1) for $\bar{\Gamma}_c$ > 1.4. This implies that layered media characterized by a high interface work of adhesion not only exhibit a higher resistance against interface delamination but also a greater affinity for crack closure.

Fig. 12 shows that the crack-tip opening displacement after jump-out β increases monotonically with the interface work of adhesion $\bar{\Gamma}_c$ for $\bar{Y}$ = 0.4, $\bar{\sigma}_c$ = 0.075, and $\bar{\delta}_{min}$ = –1.0. This trend can be attributed to the decrease of the film deflection before jump-out with the increase of the interface work of adhesion. Indeed, as shown in Fig. 12, the film deflection at the crack-tip location $\bar{\Delta}_f$ before jump-out decreases with the increase of $\bar{\Gamma}_c$. Because this implies a decrease of $\frac{U_f}{U_s}$ (for fixed U_s) with increasing $\bar{\Gamma}_c$, the increasing trend of β seen in Fig. 12 can be explained by Eq. (7).

In the previous simulation cases, the interfacial work of adhesion was assumed to be lower than the work of adhesion of the sphere/film contact system (i.e., $\bar{\Gamma}_c \ll 1$) because the main objective of the present analysis is to examine adhesion-induced film delamination in layered media, which is important for film/substrate interfaces characterized by a work of adhesion lower than that of the contact interface. For interface work of adhesion much higher than the surface work of adhesion (i.e., $\bar{\Gamma}_c \gg 1$), Xia et al. (2007) have shown that film delamination may result from interfacial shear failure during loading due to the elastic mismatch across the film/substrate interface or interfacial tensile failure during unloading due to excessive plastic deformation in the substrate accumulated during loading. For the same reason stated above, the simulation results presented in the following section are for an interface cohesive strength less than the adhesive stress at the surface (i.e., $\bar{\sigma}_c \ll 1$).

3.4. Effect of cohesive strength

Figs. 13(a) and 13(b) show the surface force $\overline{P}$ and corresponding film-substrate separation below the center of contact $\overline{\Delta}_o$, respectively, as functions of the surface separation $\overline{\delta}$ for $\overline{\Gamma}_c$ = 0.125, $\overline{Y}$ = 0.4, $\overline{\sigma}_c$ = 0.015, 0.075, and 0.2, and $\overline{\delta}_{\min}$ = –1.0. As expected, the stiffness increases with the cohesive strength. For a relatively low cohesive strength ($\overline{\sigma}_c$ = 0.015), the unloading response does not show any distinguishable discontinuity until the commencement of jump-out, implying a secondary effect of interface damage to the overall contact stiffness. For an intermediate cohesive strength ($\overline{\sigma}_c$ = 0.075), however, the unloading behavior shows that the contact stiffness during damage (crack) initiation (BC) differs significantly from that obtained during the evolution of interface damage (delamination) (CD). Discontinuities in the surface force and the film-substrate separation (CD in Figs. 13(a) and 13(b), respectively) responses occur only for a relatively high cohesive strength ($\overline{\sigma}_c$ = 0.2), indicating unstable crack initiation at the film/substrate interface. This behavior can be interpreted in terms of the dimensionless parameter $\Lambda = \frac{E^* h_g}{a\sigma_c}$, where a is the contact radius at minimum surface separation (Gao and Bower, 2004), representing the ratio of the layered medium stiffness to the film/substrate interface stiffness. Analytical and numerical results of the former study show that unstable crack initiation is characterized by low Λ values. This is in good agreement with the finding that a high $\overline{\sigma}_c$ leads to unstable crack initiation. Because a low $\overline{\sigma}_c$ produces a high Λ value (i.e., layered medium stiffness higher than that of the film/substrate interface), the effect of the cohesive interface on the overall unloading response is secondary compared to the elastic deflection of the film. This suggests that damage (cracking) at a low cohesive strength interface does not affect the continuity of the unloading response up to the instant of jump-out, in agreement with the results for $\overline{\sigma}_c$ = 0.015 and 0.075 shown in Fig. 13(a).

Fig. 14(a) shows the radius of the fictitious crack $\overline{a}_{fc}$ and the residual fictitious crack $\overline{a}_{fc}^{res}$ as functions of the cohesive strength $\overline{\sigma}_c$ for $\overline{\Gamma}_c$ = 0.125, $\overline{Y}$ = 0.4, and $\overline{\delta}_{\min}$ = –1.0. It is noted that $\overline{a}_{fc}$ decreases monotonically with the increase of $\overline{\sigma}_c$ because the critical stress for damage initiation increases with $\overline{\sigma}_c$. However, $\overline{a}_{fc}^{res}$ exhibits a non-monotonic dependence on $\overline{\sigma}_c$, because of the partial closure of

the fictitious crack, asymptotically approaching to $\bar{a}_{fc}$ with the increase of $\bar{\sigma}_c$. Fig. 14(b) shows that the closure of the fictitious crack *c* after full unloading (jump-out) decreases sharply with the increase of $\bar{\sigma}_c$, asymptotically approaching to zero. This trend can be explained by considering that $h_c \propto \sigma_c^{-1}$ for fixed $\bar{\Gamma}_c$ (Eq. (5)). Thus, the decrease of the crack closure with the increase of the cohesive strength can be attributed to the simultaneous decrease of h_c, which is conducive to failure (cracking).

Fig. 15 shows the crack-tip opening displacement after jump-out β and the film deflection at the crack-tip location before jump-out $\bar{\Delta}_f$ as functions of the cohesive strength $\bar{\sigma}_c$ for $\bar{\Gamma}_c$ = 0.125, $\bar{Y}$ = 0.4, and $\bar{\delta}_{\min}$ = –1.0. The decrease of β with the increase of $\bar{\sigma}_c$ can be interpreted as a decrease of the interfacial fracture resistance with the increase of the cohesive strength. This counterintuitive result can be explained by considering the increase of $\bar{\Delta}_f$ with $\bar{\sigma}_c$, implying an increase of $\frac{U_f}{U_s}$, which, in view of Eq. (7), explains the decrease of β with the increase of $\bar{\sigma}_c$.

3.5. Effect of initial crack size

In all previous simulation cases, the film/substrate interface was assumed to be flawless, i.e., no preexisting defect. The effect of a penny-shaped crack of radius $\bar{a}_i$ at the film/substrate interface below the center of contact on the resulting surface force and contact behavior is examined in this section. Figs. 16(a) and 16(b) show the surface force $\bar{P}$ and the corresponding film-substrate separation below the center of contact $\bar{\Delta}_o$, respectively, as functions of the surface separation $\bar{\delta}$ for $\bar{\Gamma}_c$ = 0.125, $\bar{Y}$ = 0.4, $\bar{\sigma}_c$ = 0.015, $\bar{\delta}_{\min}$ = – 1.0, and $\bar{a}_i$ = 1, 4, and 8. The increase of the surface separation at the instants of jump-in and jump-out with the crack radius is attributed to the decrease of the stiffness of the layered medium with the increase of the crack radius. The loading paths (solid lines) for different $\bar{a}_i$ values begin to gradually overlap after jump-in as the interface is increasingly compressed. The initial unloading response (dashed lines) is not affected by the variation of $\bar{a}_i$ because the interface is under compression ($\bar{\Delta}_o$ = 0). However, beyond a critical surface separation ($\bar{\delta} >$ –0.75) the unloading behavior shows a dependence

on $\bar{a}_i$ (Fig. 16(a)) and the film-substrate separation at the instant of jump-out significantly increases with crack radius (Fig. 16(b)).

Fig. 17 shows the surface separation at jump-in $\bar{\delta}_{in} = \frac{\delta_{in}}{t}$ and jump-out $\bar{\delta}_{out} = \frac{\delta_{out}}{t}$ as functions of the initial crack radius $\bar{a}_i$ for $\bar{\Gamma}_c$ = 0.125, $\bar{Y}$ = 0.4, $\bar{\sigma}_c$ = 0.075, and $\bar{\delta}_{min}$ = –1.0. For a very small initial crack (i.e., $\bar{a}_i$ < 2), $\bar{\delta}_{in}$ and $\bar{\delta}_{out}$ are almost constant, implying that adhesion-induced contact instabilities are not affected by a relatively small interfacial defect. However, above a critical defect size (e.g., $\bar{a}_i$ > 2.5), $\bar{\delta}_{in}$ and $\bar{\delta}_{out}$ demonstrate a linear dependence on $\bar{a}_i$. This suggests that the size of a preexisting interfacial defect can be correlated to the surface separation at the instant of jump-in or jump-out, in particular the latter that shows a higher sensitivity to defect size, as indicated by the larger slope of the $\bar{\delta}_{out}$ versus $\bar{a}_i$ linear fit shown in Fig. 17.

3.6. Implications of the present analysis

The results of the present analysis have direct implications in the reliability of microprobe-based techniques (e.g., atomic force microscopy and nanoindentation) and the accurate measurement of the nanomechanical/tribological properties of thin films (e.g., diamond-like films used as protective overcoats of hard disks). Adhesion-induced film detachment (delamination) is an alternative method to the peeling-off test, which is traditionally used to quantify film-substrate adhesion, especially for difficult to handle ultrathin films. Moreover, for a given loading history (indentation depth), the properties of the film/substrate interface, such as the work of adhesion and the cohesive strength, can be predicted from the measured residual film deflection, the residual crack/cohesive zone radius, and the crack-tip opening displacement. In addition, as shown in the previous section, the size of a defect (crack) at the film/substrate interface can be determined by tracking the commencement of contact instabilities.

The selection of the tip material and geometry is critical to the investigation of interface delamination in layered systems. In particular, the surface energy of the tip must be sufficiently high to preferentially induce interface delamination, but also allow for surface detachment to occur without

inducing film fracture due to excessive bending. Moreover, the tip radius should be sufficiently large to prevent gross plastic deformation and allow the detection of the adhesion force, which is linearly proportional to the tip radius (Johnson et al., 1971; Derjaguin et al., 1975). However, caution should be exercised in the selection of the tip radius because a larger tip may require a stiffer probe, which could compromise the capability of the instrument to apply loads resulting in predominantly elastic contact deformation. In addition, roughness effects introduced by a large tip may dramatically decrease the adhesion force and, in turn, the measurement sensitivity and tracking of the contact instabilities.

4. Conclusions

A finite element analysis of a rigid sphere in adhesive contact with a half-space consisting of an elastic film and an elastic-plastic semi-infinite substrate was performed to elucidate damage (crack) initiation and evolution (delamination) at the film/substrate interface. Surface adhesion was simulated by nonlinear springs obeying a force-displacement constitutive relation derived from the LJ potential. The film/substrate interface was modeled as an irreversible cohesive zone with a fixed cohesive strength and work of adhesion. The overall contact behavior was analyzed by tracking the evolution of the surface force and the surface separation at the film/substrate interface during a full load-unload cycle.

Differences in the deformation response were most pronounced during unloading. Variations in the surface force and contact stiffness during unloading correlated with the initiation and development of interfacial damage (cracking). Re-yielding in the elastic-plastic substrate occurred only during damage initiation in the course of unloading, resulting in the formation of a cohesive zone at the film/substrate interface. Substrate plasticity resulted in the irreversible downward deflection of the partially delaminated elastic film and the formation of a residual cohesive zone at the film/substrate interface, which produced tensile stresses at the tip of the interfacial crack after full unloading (jump-out). The dependence of the crack-tip opening displacement on the minimum surface separation (maximum compressive force) was interpreted in the context of energy release rate considerations before and after the occurrence of jump-

out. The crack-tip opening displacement increased whereas the residual deflection (bending) of the elastic film decreased with the increase of the minimum surface separation.

Different unloading mechanisms were encountered, depending on the yield strength of the elastic-plastic substrate. For a low-strength substrate, interface delamination was not observed during unloading, while for a substrate of intermediate strength, damage (crack) initiation and failure (delamination) at the film/substrate interface occurred during unloading, leading to the formation of a residual crack upon jump-out. For a high-strength substrate, deformation during loading was essentially elastic and the interface crack formed during unloading exhibited almost complete closure upon jump-out.

The work of adhesion of the film/substrate interface affected the contact behavior only during unloading. In particular, both the surface force and the contact stiffness were influenced by the evolution of interfacial damage during unloading only in the case of a film/substrate interface possessing a relatively low work of adhesion. Crack closure and the crack-tip opening displacement after full unloading (jump-out) increased with work of adhesion of the film/substrate interface.

The cohesive strength exhibited a significant effect on both loading and unloading behaviors. Unstable crack initiation occurred only for a high cohesive strength. This trend was interpreted in terms of a dimensionless parameter representing the ratio of the layered medium stiffness to the stiffness of the film/substrate interface. Crack closure and the crack-tip opening displacement after full unloading (jump-out) increased with the decrease of the cohesive strength due to the enhancement of the closure of the cohesive zone and the increase of the critical surface separation for interfacial failure, respectively.

The effect of an initial crack at the film/substrate interface on the contact behavior was found to be significant only during unloading. Although the effect of the initial crack on the initial unloading response was insignificant, the surface force demonstrated a dependence on the initial crack radius (size) at a later stage of unloading. Above a critical crack radius, surface separation at the instant of jump-in or jump-out increased linearly with the radius of the initial crack at the film/substrate interface.

References

Anderson, T.L., 1995. *Fracture Mechanics: Fundamentals and Applications*, second edition, CRC Press, Boca Raton, FL.

Bagchi, A., Evans, A.G., 1996. The mechanics and physics of thin film decohesion and its measurement. Interface Science 3, 169–193.

Carpick, R.W., Ogletree, D.F., Salmeron, M., 1999. A general equation for fitting contact area and friction vs load measurements. Journal of Colloid and Interface Science 211, 395–400.

Chai, H., 2003. Fracture mechanics analysis of thin coatings under spherical indentation. International Journal of Fracture 119, 263–285.

Chen, L., Yeap, K.B., Zeng, K.Y., Liu, G.R., 2009, Finite element simulation and experimental determination of interfacial adhesion properties by wedge indentation. Philosophical Magazine 89, 1395–1413.

Derjaguin, B.V., Muller, V.M., Toporov, Y.P., 1975. Effect of contact deformations on the adhesion of particles. Journal of Colloid and Interface Science 53, 314–326.

Drory, M.D., Hutchinson, J.W., 1996. Measurement of the adhesion of a brittle film on a ductile substrate by indentation. Proceedings of the Royal Society of London Series A 452, 2319–2341.

Du, Y., Chen, L., McGruer, N.E., Adams, G.G., Etsion, I., 2007. A finite element model of loading and unloading of an asperity contact with adhesion and plasticity. Journal of Colloid and Interface Science 312, 522–528.

Eid, H., Joshi, N., McGruer, N.E., Adams, G.G., 2011. A model of contact with adhesion of a layered elastic-plastic microsphere with a rigid flat surface. ASME Journal of Tribology 133, 031406-1–031406-5.

Feng, J.Q., 2001. Adhesive contact of elastically deformable spheres: a computational study of pull-off force and contact radius. Journal of Colloid and Interface Science 238, 318–323.

Gao, Y.F., Bower, A.F., 2004. A simple technique for avoiding convergence problems in finite element simulations of crack nucleation and growth on cohesive interfaces. Modelling and Simulation in Materials Science and Engineering 12, 453–463.

Greenwood, J.A., 1997. Adhesion of elastic spheres. Proceedings of the Royal Society of London Series A 453, 1277–1297.

Johnson, K.L., Kendall, K., Roberts, A.D., 1971. Surface energy and the contact of elastic solids. Proceedings of the Royal Society of London Series A 324, 301–313.

Kadin, Y., Kligerman, Y., Etsion, I., 2008. Loading-unloading of an elastic-plastic adhesive spherical microcontact. Journal of Colloid and Interface Science 321, 242–250.

Komvopoulos, K., 1996. Surface engineering and microtribology for microelectromechanical systems. Wear 200, 305–327.

Komvopoulos, K., 2000. Head-disk interface contact mechanics for ultrahigh density magnetic recording. Wear 238, 1–11.

Komvopoulos, K., 2003. Adhesion and friction forces in microelectromechanical systems: mechanisms, measurement, surface modification techniques, and adhesion theory. Journal of Adhesion Science and Technology 17, 477–517.

Marshall, D.B., Evans, A.G., 1984. Measurement of adherence of residually stressed thin films by indentation. I. Mechanics of interface delamination. Journal of Applied Physics 56, 2632–2638.

Maugis, D., 1992. Adhesion of spheres: the JKR-DMT transition using a Dugdale model. Journal of Colloid and Interface Science 150, 243–269.

Muller, V.M., Yushchenko, V.S., Derjaguin, B.V., 1980. On the influence of molecular forces on the deformation of an elastic sphere and its sticking to a rigid plane. Journal of Colloid and Interface Science 77, 91–101.

Smallwood, S.A., Eapen, K.C., Patton, S.T., Zabinski, J.S., 2006. Performance results of MEMS coated with a conformal DLC. Wear 260, 1179–1189.

Song, Z., Komvopoulos, K., 2011. Adhesion-induced instabilities in elastic and elastic-plastic contacts during single and repetitive normal loading. Journal of the Mechanics and Physics of Solids 59, 884–897.

Song, Z., Komvopoulos, K., 2013. Adhesive contact of elastic-plastic layered media: Effective Tabor parameter and mode of surface separation. ASME Journal of Applied Mechanics 80, 0211022(1) – 0211022(9).

Tabor, D., 1977. Surface forces and surface interactions. Journal of Colloid and Interface Science 58, 2–13.

Tvergaard, V., Hutchinson, J.W., 1994. Toughness of an interface along a thin ductile layer joining elastic solids. Philosophical Magazine A 70, 641–656.

Tvergaard, V., Hutchinson, J.W., 1996. Effect of strain-dependent cohesive zone model on predictions of crack growth resistance. International Journal of Solids and Structures 33, 3297–3308.

Wu, J.-J., 2008. Easy-to-implement equations for determining adhesive contact parameters with the accuracy of numerical simulations. Tribology Letters 30, 99–105.

Xia, S.M., Gao, Y.F., Bower, A.F., Lev, L.C., Cheng, Y.-T., 2007. Delamination mechanism maps for a strong elastic coating on an elastic-plastic substrate subjected to contact loading. International Journal of Solids and Structures 44, 3685–3699.

Nomenclature

a_c crack radius

$\bar{a}_c$ dimensionless crack radius $\left(=\frac{a_c}{t}\right)$

a_i radius of the initial crack

$\bar{a}_i$ dimensionless radius of the initial crack $\left(=\frac{a_i}{t}\right)$

a_{fc} radius of the fictitious crack

$\bar{a}_{fc}$ dimensionless radius of the fictitious crack $\left(=\frac{a_{fc}}{t}\right)$

a_{fc}^{res} radius of the residual fictitious crack

$\bar{a}_{fc}^{res}$ dimensionless radius of the residual fictitious crack ($= \frac{a_{fc}^{res}}{t}$)

CTOD crack-tip opening displacement after jump-out (full unloading)

c closure of the residual fictitious crack $\left(= 1 - \left(\frac{a_{fc}^{res}}{a_{fc}}\right)^2\right)$

d node-to-node distance (mesh size)

E_f film elastic modulus

E_s substrate elastic modulus

E^* effective elastic modulus

E_1, E_2 elastic modulus of spheres (1) and (2)

U_f elastic strain energy in the film

U_s plastic strain energy in the substrate

G energy release rate

h interfacial separation within the cohesive zone

h^* effective interfacial separation for damage (crack) initiation within the cohesive zone

h_c interfacial separation for failure (delamination) within the cohesive zone or crack-tip surface separation

h_{ef} effective interfacial separation within the cohesive zone

h_{fc} interfacial separation at the tip of the fictitious crack

h_{fc}^{res} interfacial separation at the tip of the residual fictitious crack

k interface stiffness

n normal direction at the film/substrate interface

P surface force

$\bar{P}$ dimensionless surface force $\left(= \frac{P}{2\pi RW}\right)$

P_{off} pull-off force

$\bar{P}_{off}$ dimensionless pull-off force ($= \frac{P_{off}}{2\pi RW}$)

R reduced radius of curvature or rigid sphere radius

R_1, R_2 radius of curvature of spheres (1) and (2)

r radial coordinate

s in-plane direction at the film/substrate interface

t film thickness or in-plane direction at the film/substrate interface

W work of adhesion of adhering spheres (1) and (2) or sphere/film contact system

Y substrate yield strength

$\bar{Y}$ dimensionless substrate yield strength $\left(=\frac{Y}{\sigma_c}\right)$

z vertical coordinate

Greek symbols

β dimensionless crack-tip opening displacement (CTOD) after jump-out $\left(=\frac{\mathrm{CTOD}}{h_c}\right)$

Γ work of surface traction on conjugate relative displacement

Γ_c work of adhesion of the film/substrate interface

$\bar{\Gamma}_c$ dimensionless work of adhesion of the film/substrate interface $\left(=\frac{\Gamma_c}{W}\right)$

Δ interfacial separation before or after jump-out

$\bar{\Delta}$ dimensionless interfacial separation before or after jump-out $\left(=\frac{\Delta}{h_c}\right)$

Δ_f film deflection at the crack-tip location

$\bar{\Delta}_f$ dimensionless film deflection at the crack-tip location $\left(=\frac{\Delta_f}{h_c}\right)$

Δ_o film-substrate separation below the center of contact

$\bar{\Delta}_o$ dimensionless film-substrate separation below the center of contact $\left(=\frac{\Delta_o}{h_c}\right)$

δ surface separation

$\bar{\delta}$ dimensionless surface separation $\left(=\frac{\delta}{t}\right)$

δ_{in} surface separation at the instant of jump-in

$\bar{\delta}_{\mathrm{in}}$ dimensionless surface separation at the instant of jump-in $\left(=\frac{\delta_{\mathrm{in}}}{t}\right)$

δ_{out} surface separation at the instant of jump-out

$\bar{\delta}_{\mathrm{out}}$ dimensionless surface separation at the instant of jump-out $\left(=\frac{\delta_{\mathrm{out}}}{t}\right)$

δ_{min} minimum surface separation

$\bar{\delta}_{min}$ dimensionless minimum surface separation $\left(=\frac{\delta_{min}}{t}\right)$

δ^{res} residual film deflection at the center of contact

$\bar{\delta}^{res}$ dimensionless residual film deflection at the center of contact $\left(=\frac{\delta^{res}}{\square}h_c\right)$

ε equilibrium interatomic distance

μ Tabor parameter

ν_1 , ν_2 Poisson's ratio of spheres (1) and (2)

σ_c cohesive strength

$\bar{\sigma}_c$ dimensionless cohesive strength $\left(=\frac{\sigma_c\varepsilon}{W}\right)$

σ_{ef} effective surface traction

σ_{max} maximum tensile stress at the tip of the residual fictitious crack

σ_{zz}^{res} residual stress in the z -direction

$\bar{\sigma}_{zz}^{res}$ dimensionless residual stress in the z -direction $\left(=\frac{\sigma_{zz}^{res}}{Y}\right)$

Figure Captions

Fig. 1 Model of a rigid sphere in close proximity with a layered medium consisting of an elastic film and an elastic-plastic semi-infinite substrate.

Fig. 2 Schematic representation of effective surface traction σ_{ef} versus effective film-substrate separation h_{ef} constitutive law of a bilinear cohesive zone. Surface separation larger than h^* leads to either partial damage (point C) or full damage (point B), accompanied by the decrease of the cohesive strength σ_c.

Fig. 3 (a) Pull-off force $\bar{F}_{off}$ versus Tabor parameter μ for $E_f = E_i =$ 5–1000 GPa, $\bar{\Gamma}_c = 2.5 \times 10^{-3}$, $\bar{\sigma}_c = 1.5 \times 10^{3}$, film surface mesh size $d =$ 0.003^R, and film/substrate interface mesh size $d =$ 0.006^R, and (b) surface force $\bar{P}$ versus surface separation $\bar{\delta}$ for $E_f = E_i =$ 50 GPa, $\bar{\Gamma}_c$ = 0.25, $\bar{\sigma}_c$ = 0.15, and film/substrate interface mesh size d = 0.003^R, 0.006^R, 0.012^R, and 0.024^R.

Fig. 4 Schematics of the deformed layered medium (a) before and (b) after complete separation (jump-out) of the elastic film from the rigid sphere. Formation of a crack and a cohesive zone (gray region), partial closure of the cohesive zone (blue region), and high tensile stresses (red region) in front of the cohesive zone can be encountered at the film/substrate interface during a full load-unload cycle, depending on the material properties and the minimum surface separation (maximum compressive force).

Fig. 5 (a) Surface force $\bar{P}$ and (b) corresponding film-substrate separation below the center of contact $\bar{\Delta}_o$ versus surface separation $\bar{\delta}$ for $\bar{\Gamma}_c$ = 0.125, $\bar{Y}$ = 0.4, $\bar{\sigma}_c$ = 0.075, and $\bar{\delta}_{min}$ = –0.5, –1.0, and –1.5 (loading = solid lines; unloading = dashed lines). For clarity, characteristic points are only shown for $\bar{\delta}_{min}$ = –1.5.

Fig. 6 (a) Contours of residual $\bar{\sigma}_{22}^{res}$ stress and (b) variation of residual film deflection at the center of contact $\bar{\delta}^{res}$ with the minimum surface separation $\bar{\delta}_{min}$ for $\bar{\Gamma}_c$ = 0.125, $\bar{Y}$ = 0.4, and $\bar{\sigma}_c$ = 0.075.

Fig. 7 Crack-tip opening displacement β and film deflection at the crack-tip location $\bar{\Delta}_f$ versus minimum surface separation $\bar{\delta}_{min}$ for $\bar{\Gamma}_c$ = 0.125, $\bar{Y}$ = 0.4, and $\bar{\sigma}_c$ = 0.075.

Fig. 8 (a) Surface force $\bar{P}$ and (b) corresponding film-substrate separation below the center of contact $\bar{\Delta}_o$ versus surface separation $\bar{\delta}$ for $\bar{\Gamma}_c$ = 0.125, $\bar{Y}$ = 0.1, 1.0, and 10, $\bar{\sigma}_c$ = 0.075, and $\bar{\delta}_{min}$ = –1.0 (loading = solid lines; unloading = dashed lines).

Fig. 9 Interfacial surface separation $\bar{\Delta}$ before (dashed lines) and after (solid lines) full unloading (jump-out) versus radial distance $\bar{r}$ for $\bar{\Gamma}_c$ = 0.125, $\bar{Y}$ = 0.1, 1.0, and 10, $\bar{\sigma}_c$ = 0.075, and $\bar{\delta}_{min}$ = –1.0.

Fig. 10 (a) Surface force $\bar{P}$ and (b) corresponding film-substrate separation at the center of contact $\bar{\Delta}_o$ versus surface separation $\bar{\delta}$ for $\bar{\Gamma}_c$ = 0.125, 0.25, and 0.5, $\bar{Y}$ = 0.4, $\bar{\sigma}_c$ = 0.075, and $\bar{\delta}_{min}$ = –1.0 (loading = solid lines; unloading = dashed lines). For clarity, characteristic points are only shown for $\bar{\Gamma}_c$ = 0.125.

Fig. 11 (a) Radius of fictitious crack $\bar{a}_{fc}$ and residual fictitious crack $\bar{a}_{fc}^{res}$ and (b) closure of the residual fictitious crack c versus work of adhesion of the film/substrate interface $\bar{\Gamma}_c$ for $\bar{Y}$ = 0.4, $\bar{\sigma}_c$ = 0.075, and $\bar{\delta}_{min}$ = –1.0.

Fig. 12 Crack-tip opening displacement β and film deflection at the crack-tip location $\bar{\Delta}_f$ versus work of adhesion of the film/substrate interface $\bar{\Gamma}_c$ for $\bar{Y}$ = 0.4, $\bar{\sigma}_c$ = 0.075, and $\bar{\delta}_{min}$ = –1.0.

Fig. 13 (a) Surface force $\bar{P}$ and (b) corresponding film-substrate separation at the center of contact $\bar{\Delta}_o$ versus surface separation $\bar{\delta}$ for $\bar{\Gamma}_c$ = 0.125, $\bar{Y}$ = 0.4, $\bar{\sigma}_c$ = 0.015, 0.075, and 0.2, and

$\bar{\delta}_{min}$ = –1.0 (loading = solid lines; unloading = dashed lines). Characteristic points are shown for $\bar{\sigma}_c$ = 0.075 and 0.2.

Fig. 14 (a) Radius of fictitious crack $\bar{a}_{fc}$ and residual fictitious crack $\bar{a}_{fc}^{res}$ and (b) closure of the residual fictitious crack c versus cohesive strength $\bar{\sigma}_c$ for $\bar{\Gamma}_c$ = 0.125, $\bar{Y}$ = 0.4, and $\bar{\delta}_{min}$ = –1.0.

Fig. 15 Crack-tip opening displacement β and film deflection at the crack-tip location $\bar{\Delta}_f$ versus cohesive strength $\bar{\sigma}_c$ for $\bar{\Gamma}_c$ = 0.125, $\bar{Y}$ = 0.4, and $\bar{\delta}_{min}$ = –1.0.

Fig. 16 (a) Surface force $\bar{P}$ and (b) corresponding film-substrate separation at the center of contact $\bar{\Delta}_o$ versus surface separation $\bar{\delta}$ for $\bar{\Gamma}_c$ = 0.125, $\bar{Y}$ = 0.4, $\bar{\sigma}_c$ = 0.075, $\bar{\delta}_{min}$ = –1.0, and $\bar{a}_i$ = 1, 4, and 8 (loading = solid lines; unloading = dashed lines).

Fig. 17 Surface separation at the instant of jump-in $\bar{\delta}_{in}$ and jump-out $\bar{\delta}_{out}$ versus initial crack radius $\bar{a}_i$ for $\bar{\Gamma}_c$ = 0.125, $\bar{Y}$ = 0.4, $\bar{\sigma}_c$ = 0.075, and $\bar{\delta}_{min}$ = –1.0.

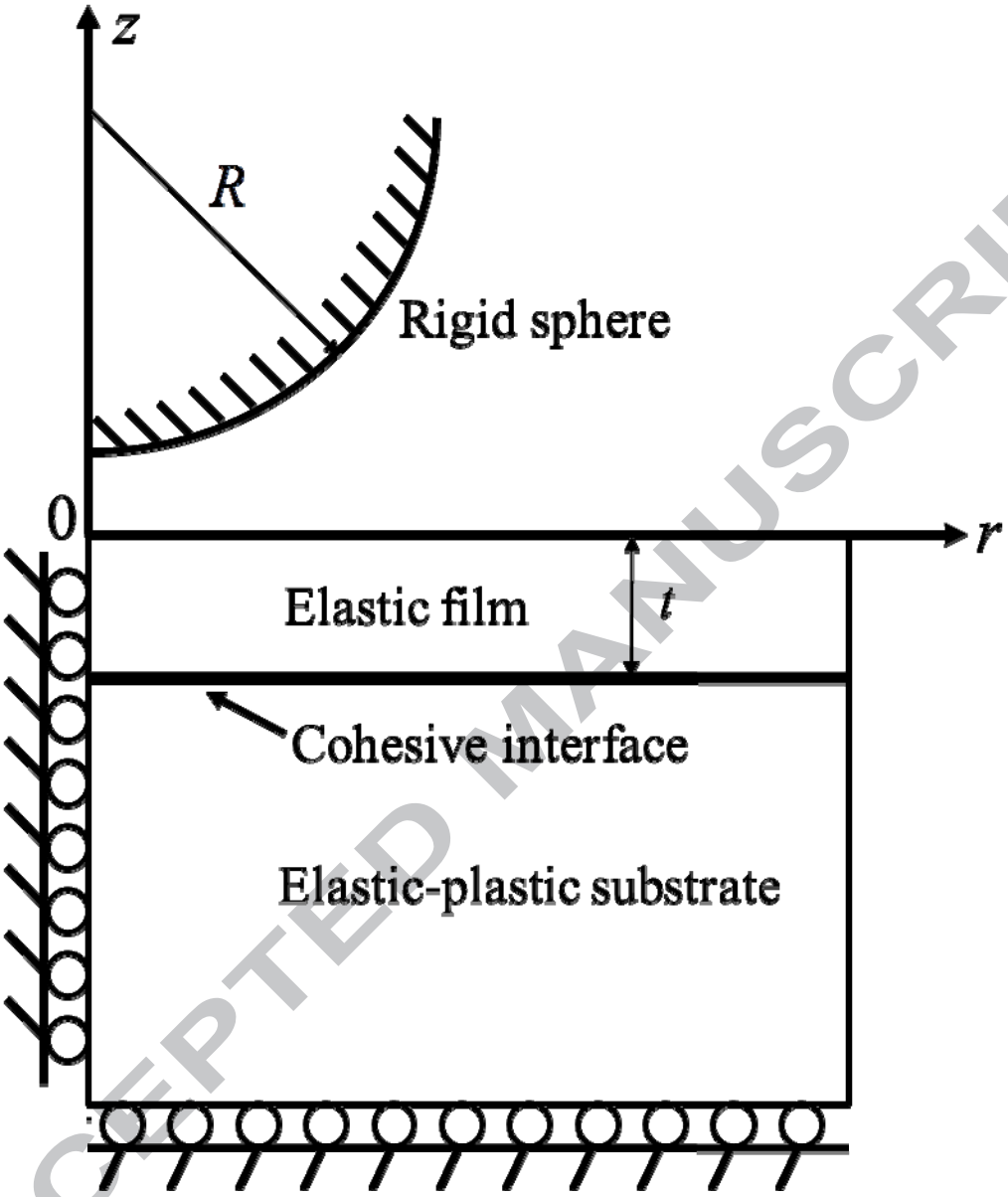

Figure 1

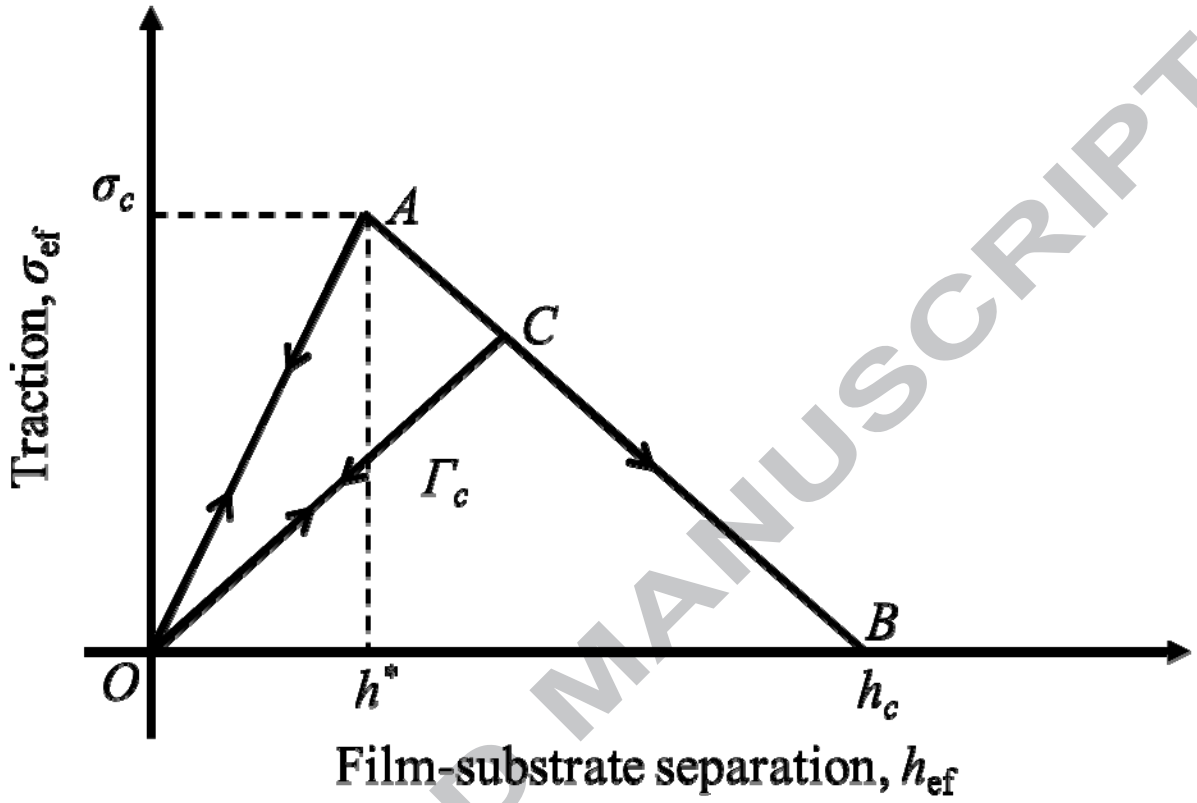

Figure 2

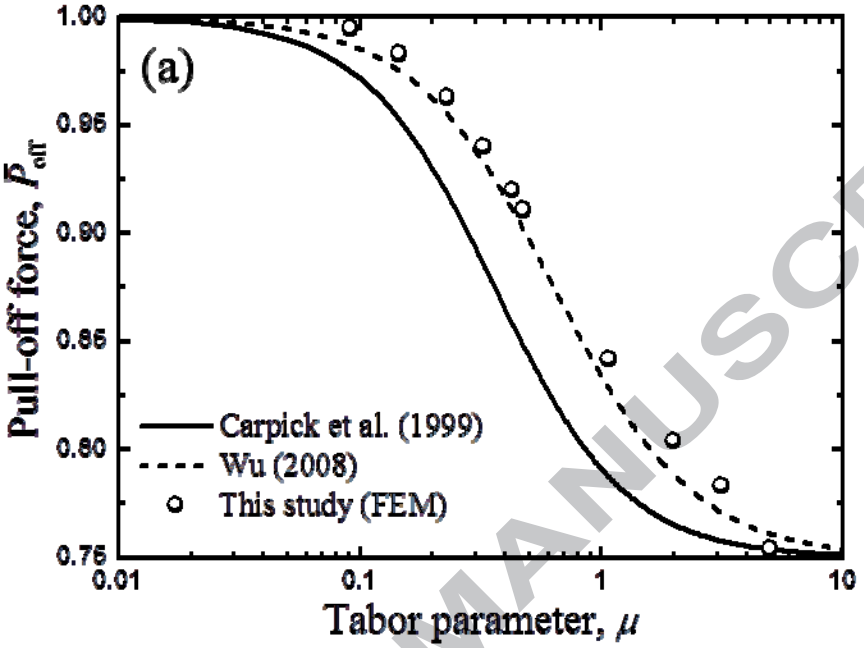

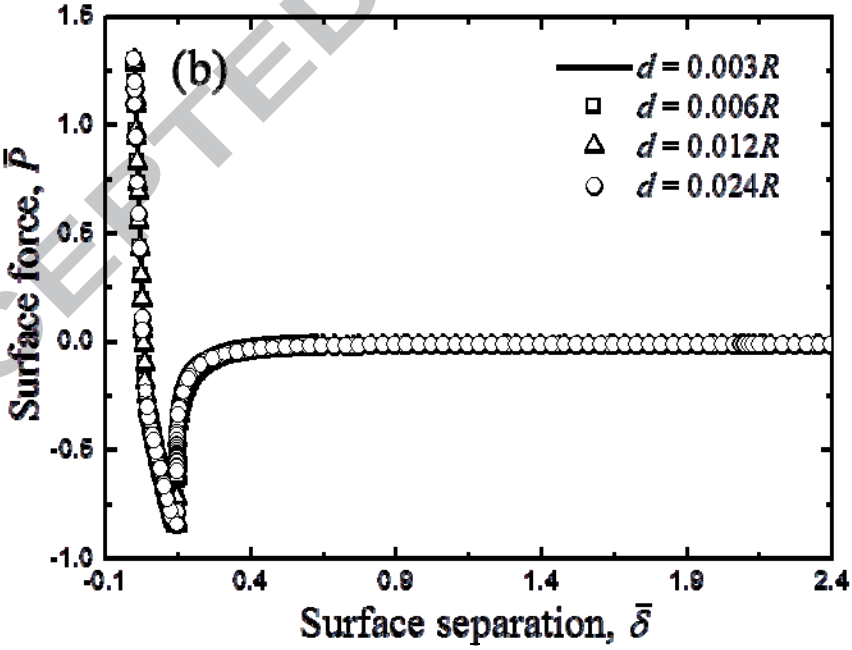

Figure 3

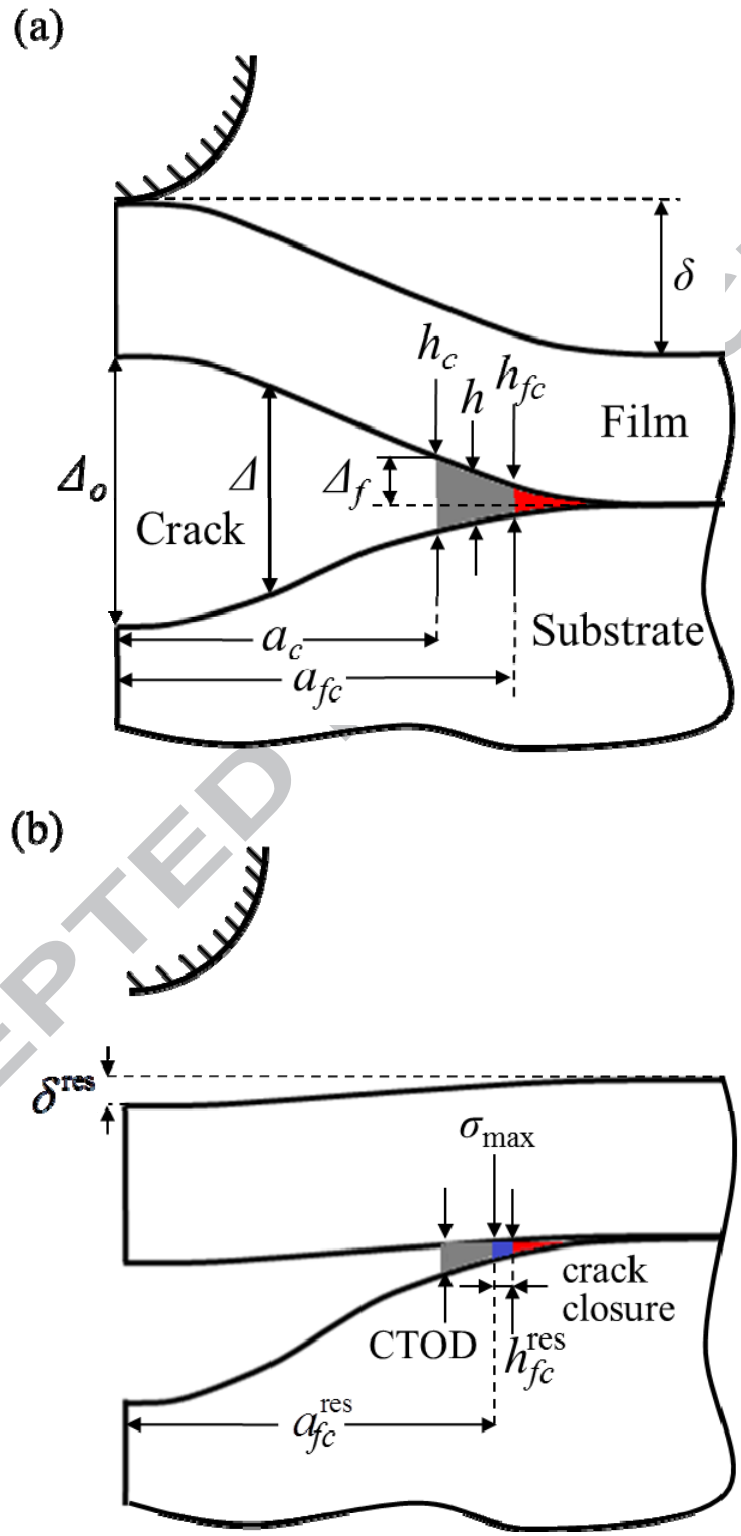

Figure 4

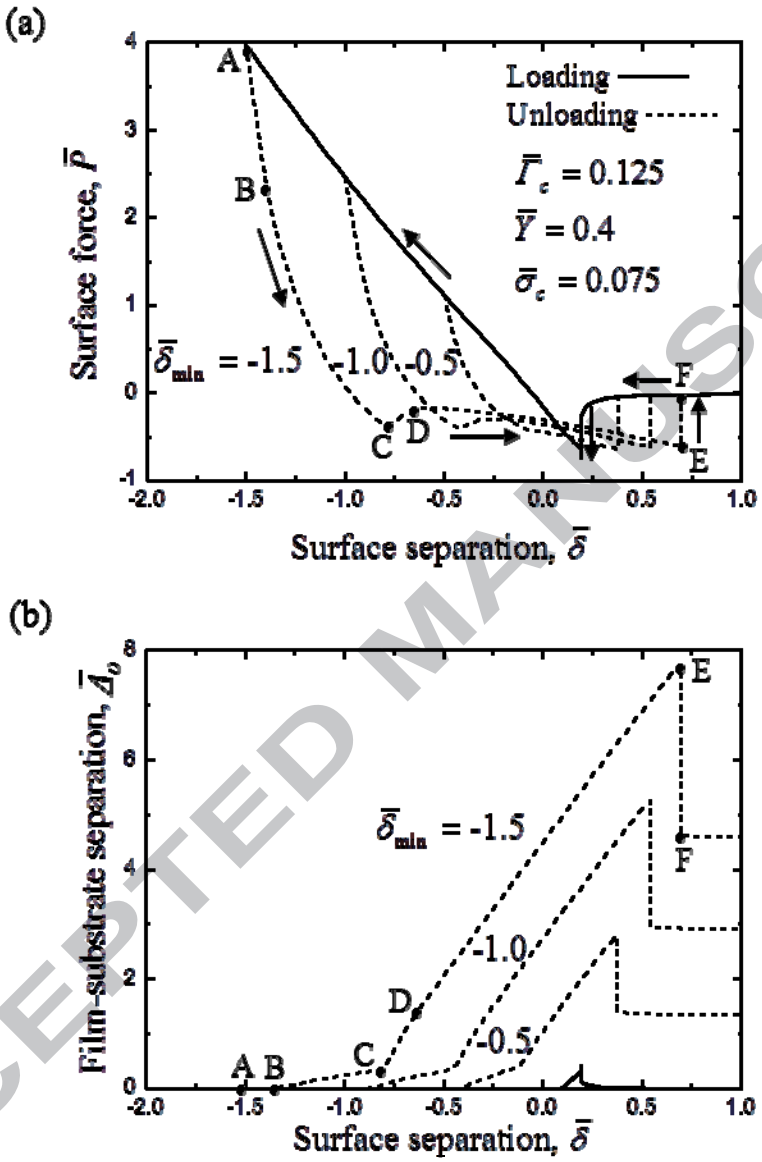

Figure 5

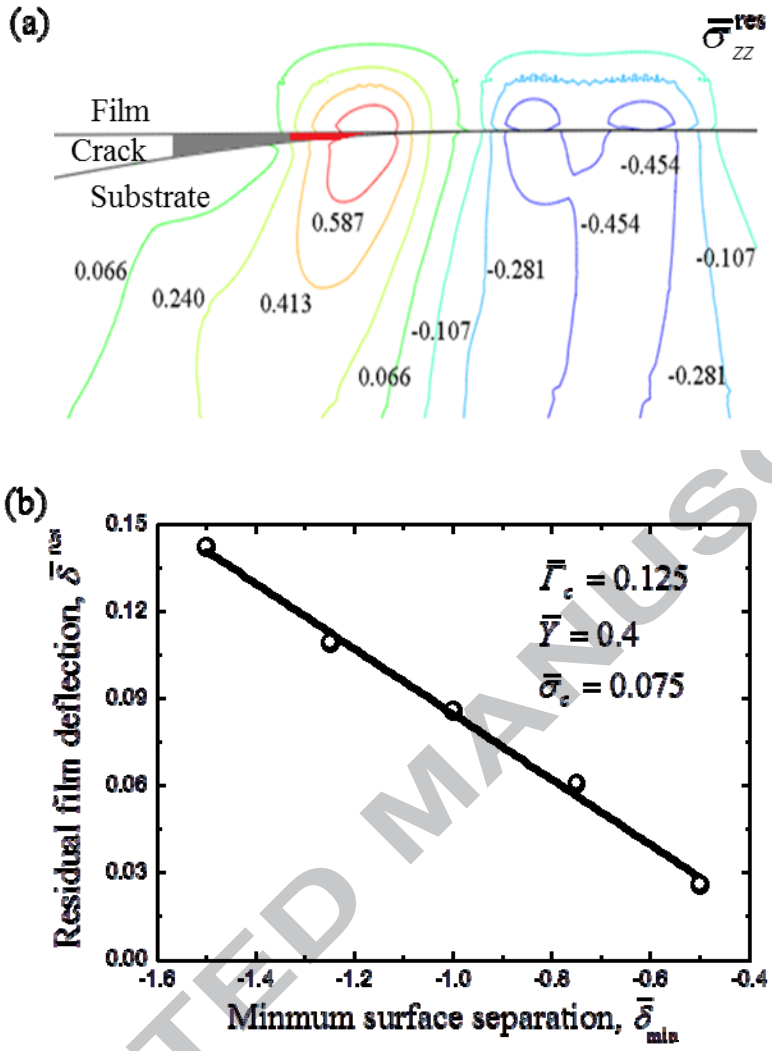

Figure 6

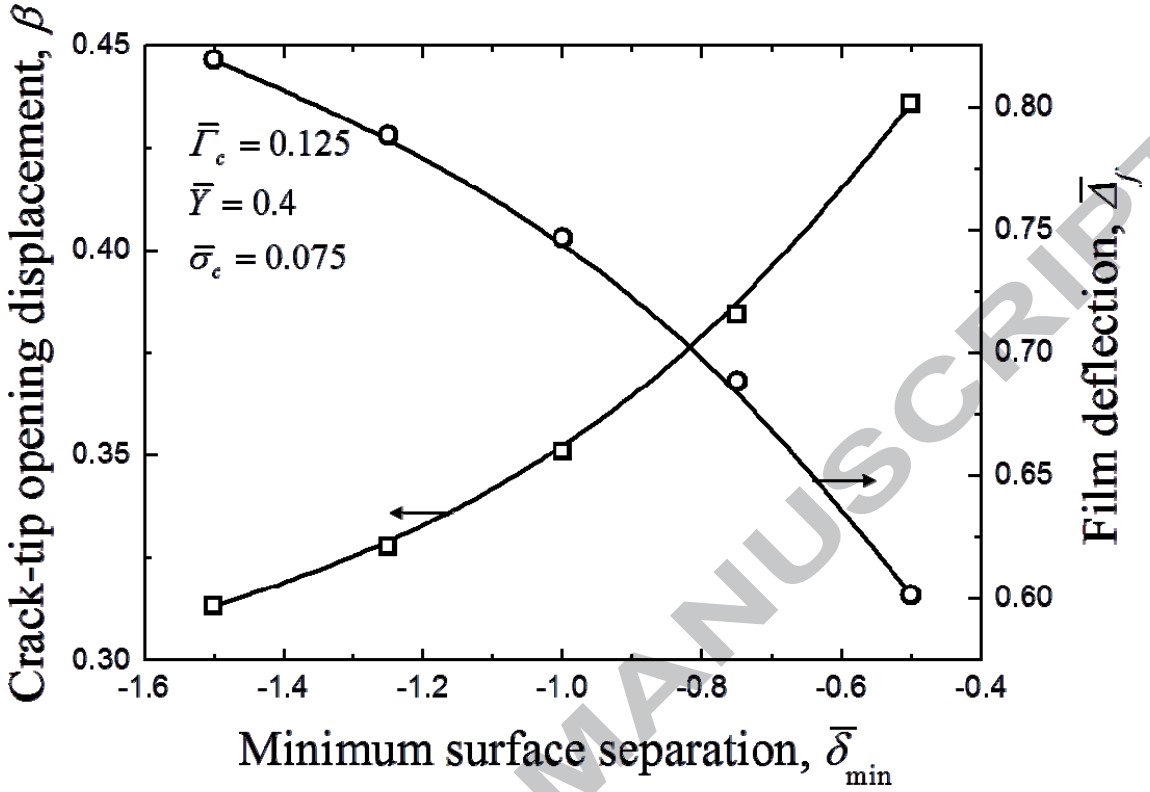

Figure 7

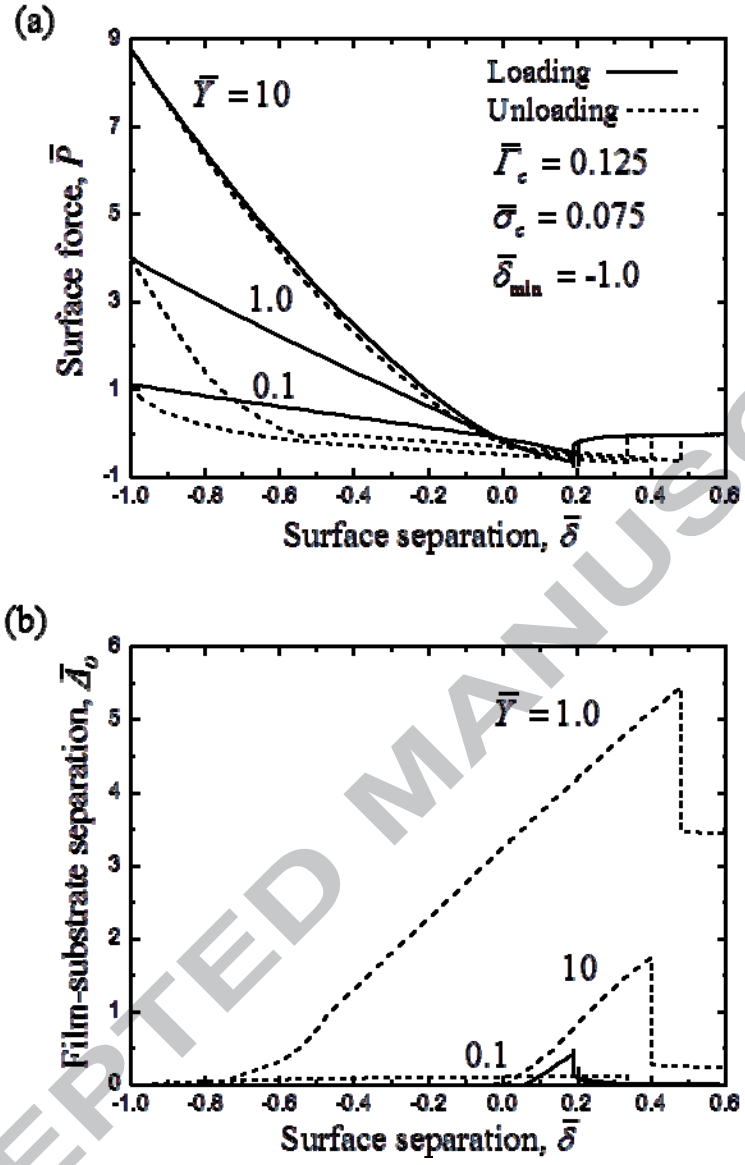

Figure 8

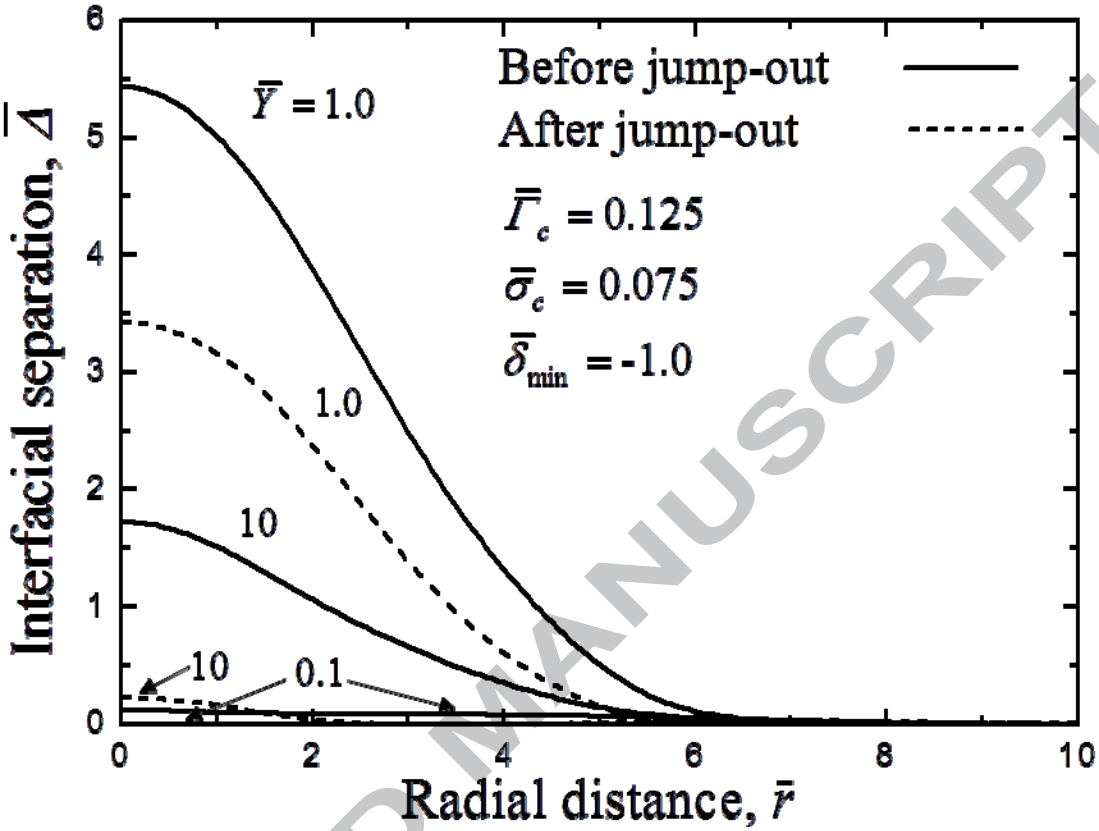

Figure 9

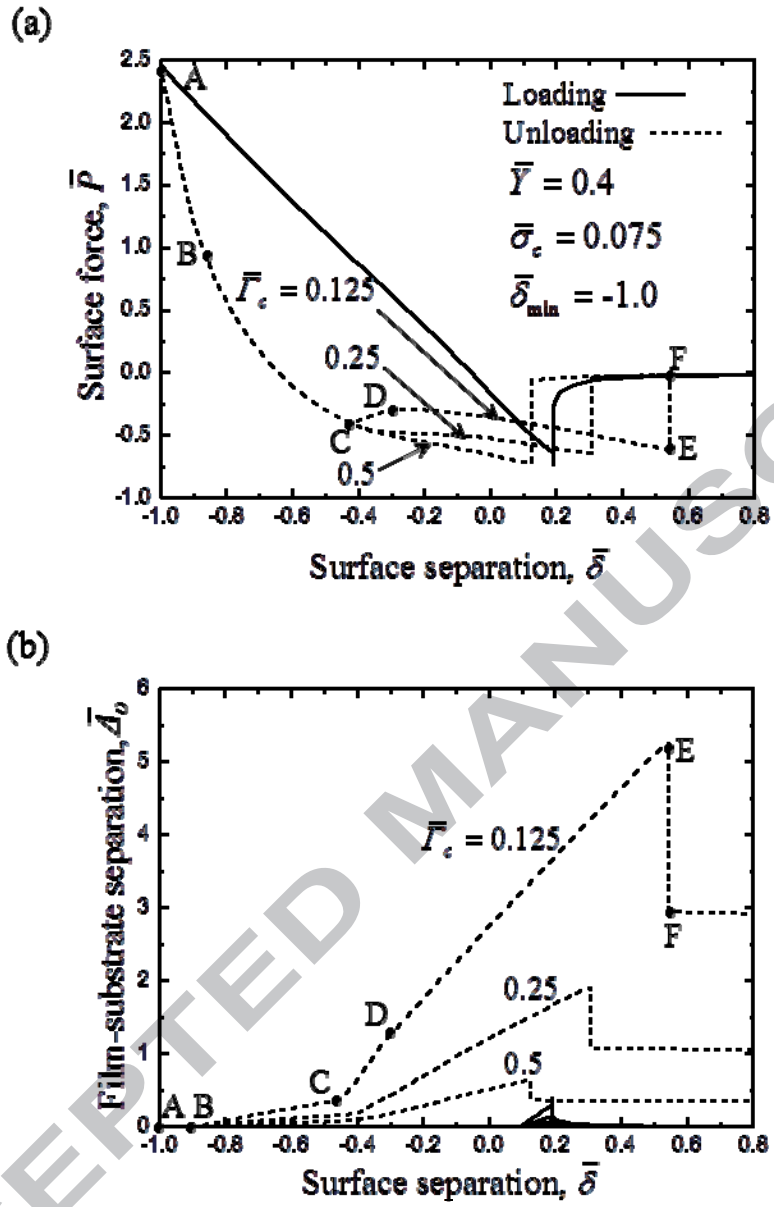

Figure 10

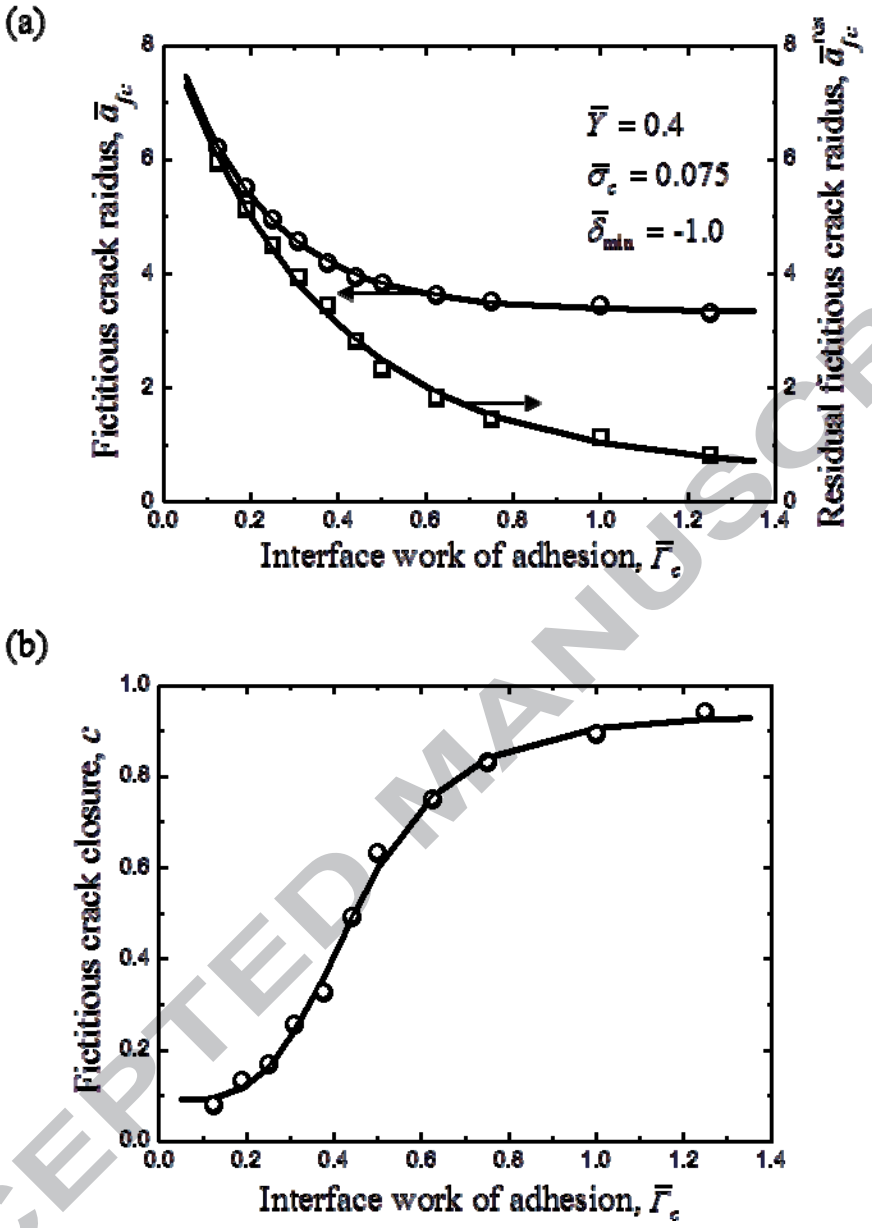

Figure 11

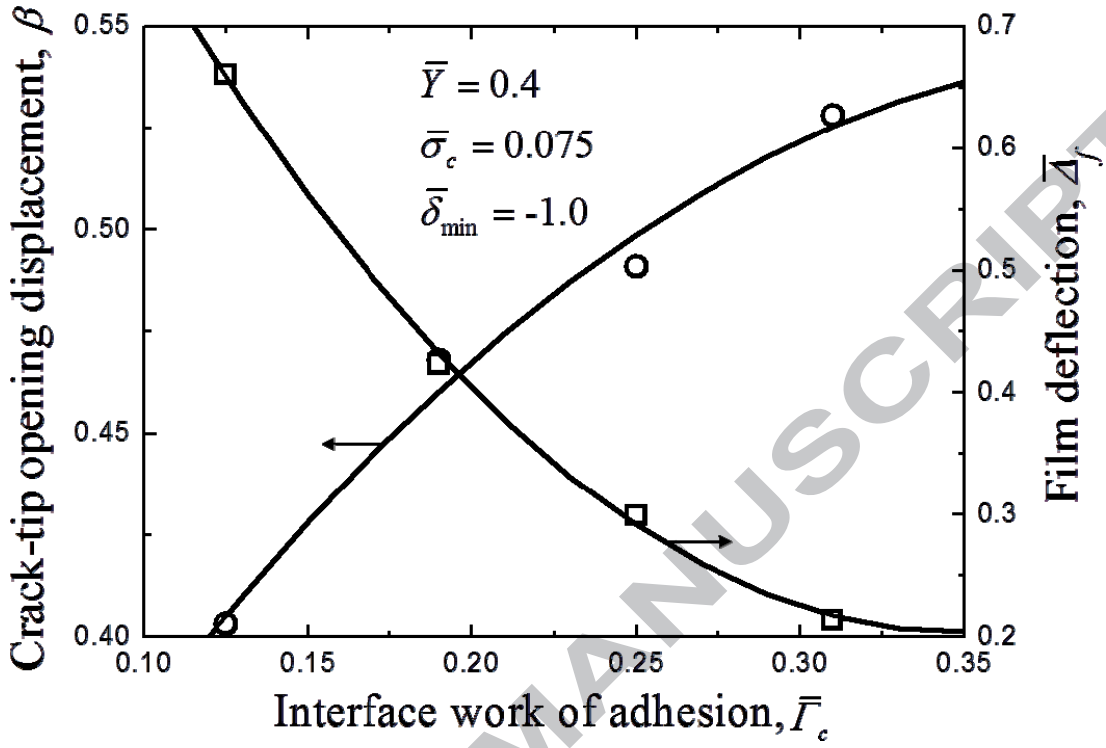

Figure 12

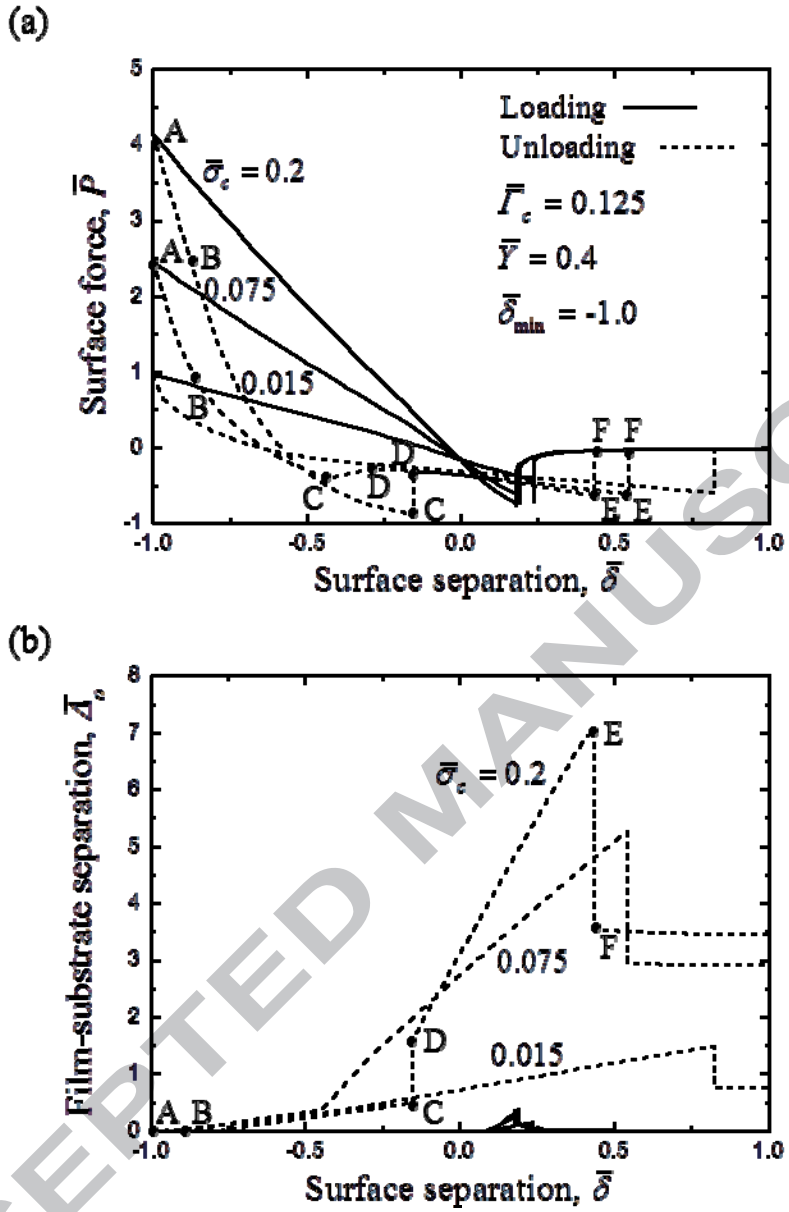

Figure 13

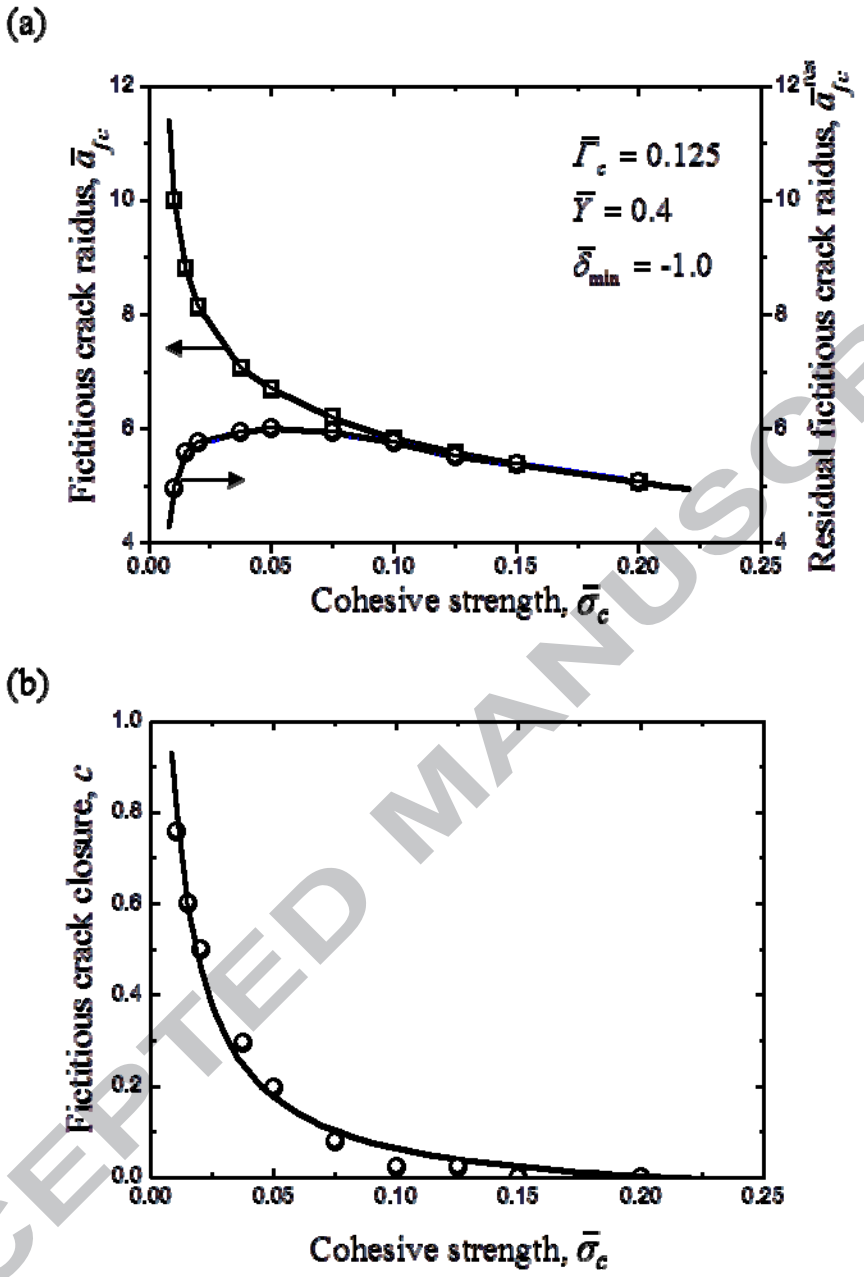

Figure 14

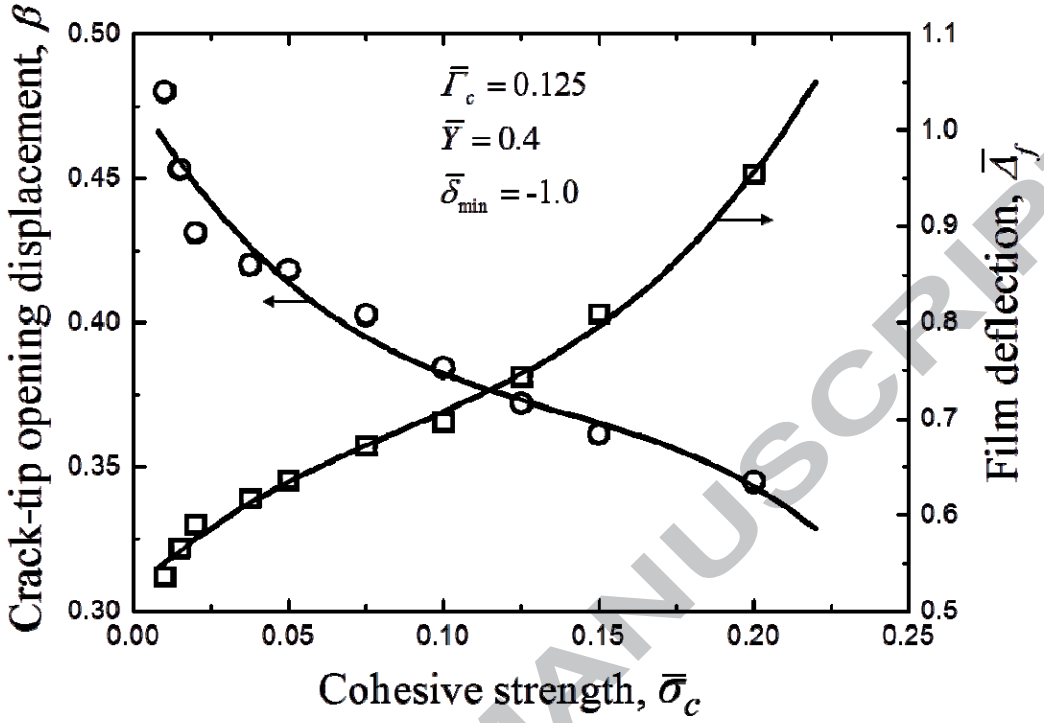

Figure 15

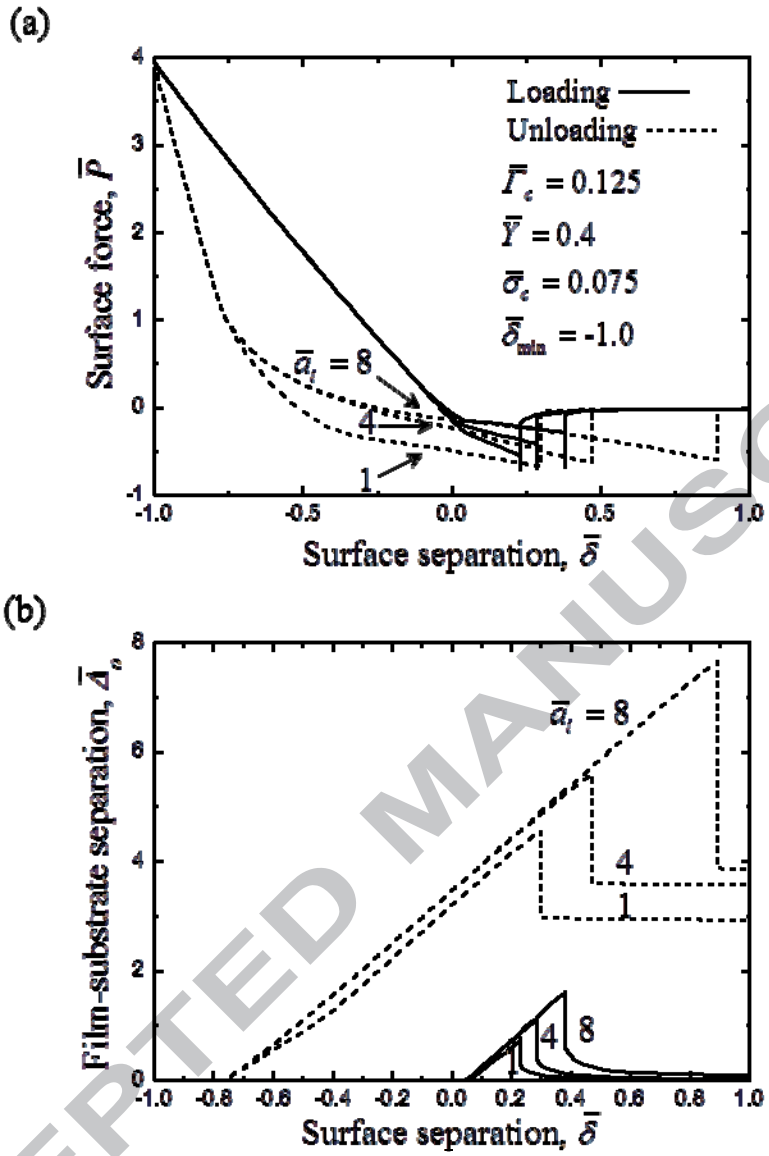

Figure 16

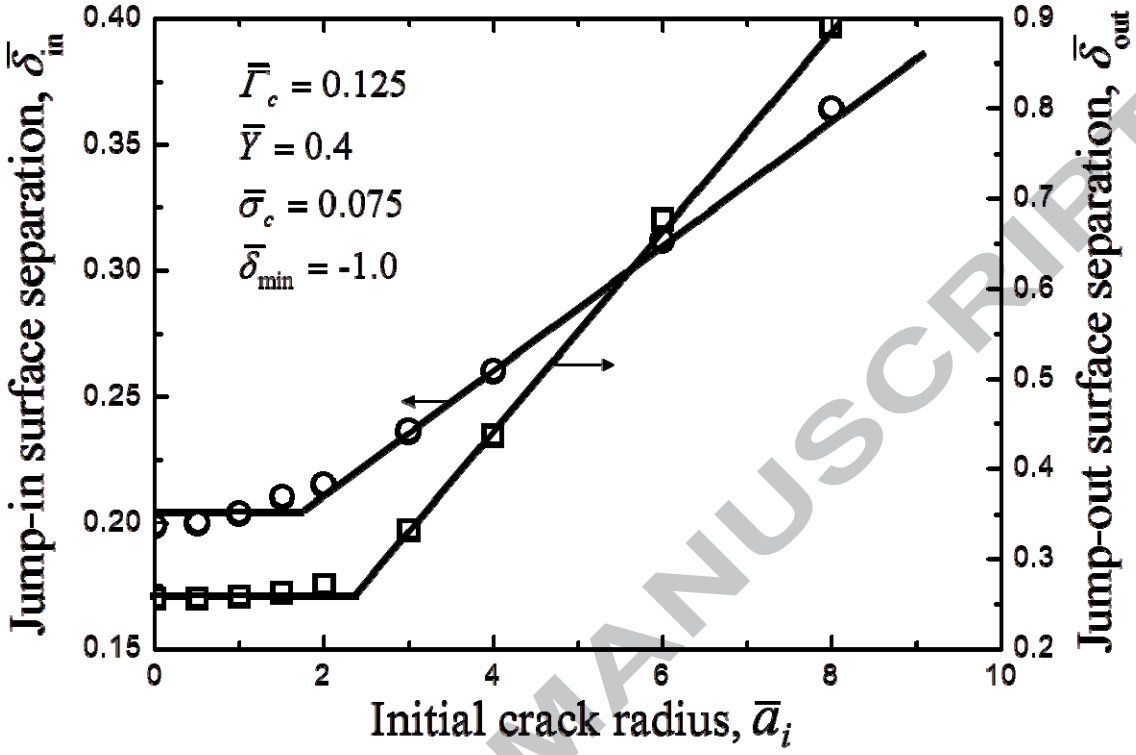

Figure 17